MASTER'S THESIS

Ray Tracing based 6G Reconfigurable Intelligent Surface Modelling

submitted by

B.Sc. Sara Sandh

presented for the degree of

Master of Science (M.Sc.) / Diplom-Ingenieurin (Dipl.-Ing.)

in

Computational Science and Engineering

Degree program:	Computational Science and Engineering (UE 066 646)
Supervised by:	Privatdoz. Dipl.-Ing. Dr.techn. Thomas Zemen

Vienna, 2023

Acknowledgements

I wish to express my deepest gratitude to my supervisor Privatdoz. Dipl.-Ing. Dr.techn. Thomas Zemen, whose consistent support, guidance, and invaluable feedback were crucial for my work. I am incredibly grateful for the introduction that he provided me to the field and for his collaborative efforts in bridging our knowledge domains. My appreciation extends to all my colleagues at the AIT Austrian Institute of Technology, especially Anja, David, Hamed, Markus, and Pascal, for warmly welcoming me into the group, creating an exceptional workplace environment, and making each lunch break cheerful. I would also like to mention my four-legged colleagues for their delightful company during short afternoon breaks.

Furthermore, I am immensely grateful to my family for their unconditional support and encouragement at every stage of my life, and to Cisse for making any country feel like home. I extend my appreciation to the wonderful friendships I have formed in Leuven and Vienna throughout my studies. Finally, I wish to express my gratitude to the female role models who have empowered me over the years, most importantly my mother, who is not only an amazing parent, but also a mentor, friend, and the best support I could ever wish for.

Abstract

Ray tracing accelerated with graphics processing units (GPUs) is an increasingly popular technique for accurate and efficient simulation of wireless communication channels. In this thesis, we extend the GPU-accelerated Ray Tracer from the AIT Austrian Institute of Technology to support the effects of reconfigurable intelligent surfaces (RISs), a modern technology aimed at solving propagation issues in the higher frequency bands of sixth-generation cellular networks (6G).

The AIT Ray Tracer implements a two-stage hybrid ray tracing method to simulate the propagation of electromagnetic waves in complex environments. We propose an approach for integrating RISs into the Ray Tracer by launching rays toward the individual RIS patch antenna elements. The electric field of the rays is manipulated and reflected upon intersection with the RIS. To evaluate the electric field, we derived a compartmentalized RIS path loss model. The flexibility of our model is easily integrated into the Ray Tracer and enables further extensions for the implementation of additional features and incorporation into more complex scenarios.

Through a comparison with measurements and an empirically established numerical model, we verified the derivation and implementation of our model. In addition, we demonstrated the capabilities of our compartmentalized model by extending the Ray Tracer to support higher-order reflections from the RIS to the receiver. We found that such components had a significant effect on the received signal strength, concluding that the extensions of advanced functionality enabled by our model play an important role in the accurate modeling of reconfigurable intelligent surfaces.

Contents

List of Figures

List of Tables

Chapter 1

Introduction

The worldwide deployment of fifth-generation (5G) mobile communication networks has enabled a wide range of applications, particularly for the internet of things (IoT) and machine-to-machine (M2M) communication. Such advances enable completely new use cases and go far beyond smartphones and traditional cellular networks. The extreme growth in global mobile data traffic over the past decade is expected to continue, and 5G is predicted to reach its capacity by 2030 through emerging technologies and innovations [1].

Sixth-generation (6G) cellular networks are currently under development to support the future demand for reliable and secure wireless connections with higher data rates and lower latencies. Such requirements are intended to enable a wide range of applications, for instance, in virtual reality, autonomous driving, and smart health monitoring [2].

Millimeter-wave frequency (mmWave) bands have already been adopted in 5G systems to address the spectrum shortage due to the increasing number of users. The use of higher frequency bands for 5G and 6G networks comes with several challenges that must be tackled. One of the biggest challenges in the mmWave band is the high propagation loss and strong attenuation of blocked transmission paths, which limit the communication distance and drastically deteriorate the signal strength [3]. Existing network technologies that can overcome the aforementioned limitations, such as relays, require increased network power consumption and hardware cost [4].

The propagation environment in wireless communication is traditionally viewed as an uncontrollable and unpredictable system that negatively affects the quality of the signal as it interacts with the environment. Recently, however, the concept of *smart radio environments*, that is, networks in which the environment actively assists in transferring and processing information, has emerged as a result of *reconfigurable intelligent surfaces (RISs)*. This new technology is an electronically controllable surface of electromagnetic (EM) material that can manipulate signals in real-time to constructively or destructively interfere at desired locations [5]. These capabilities result in numerous potential applications such as improving the signal-to-noise ratio (SNR), tackling eavesdropping [4], and assisting environmental sensing and positioning [6]. Furthermore, RISs offer particularly promising solutions to long-distance and non-line-of-sight (NLOS) propagation issues for mmWaves [5], which make them an important enabling technology for 6G wireless networks.

To achieve the full potential of RISs, several major challenges remain: real-time channel estimation, feedback of the received signal strength, control of the RIS, system optimization, and deployment, to name a few [5]. To understand the limitations and

optimize configurations, it is thus of great importance to develop accurate RIS models and numerical radio wave simulation tools.

The effects of an RIS in a given environment can be established using channel models. A wireless channel is the environment between the transmitter and receiver, through which electromagnetic waves propagate. The waves propagate according to Maxwell's equations with given boundary conditions, which can be solved numerically using deterministic channel models. The most accurate methods to solve Maxwell's equations are integral or differential formulations, such as the finite element method (FEM) or finite-difference time-domain (FDTD) method. However, their computational complexity, high memory requirements, and challenges in defining precise boundary conditions pose difficulties when employed in most environments, hence the use of approximations. The most common approximation is the high-frequency approximation, also known as ray approximation or ray tracing, in which electromagnetic waves of high frequency in relation to the dimensions of the environment are modeled as rays that follow the laws of geometrical optics [7]. In addition to reducing complexity, several acceleration methods exist to improve the performance of ray tracing. Ray tracing originates from computer graphics and is often performed using graphics processing units (GPUs) to simulate the lighting of a scene. In the past decade, GPUs have also been employed to accelerate radio propagation modeling in 3D environments [8].

The GPU-accelerated Ray Tracer from the AIT Austrian Institute of Technology, introduced in [9], is based on the NVIDIA OptiX ray tracing engine. In this thesis, the AIT Ray Tracer was extended to support the effects of RISs in complex environments. The implementation was compared against an empirically verified path loss model given in [10] and measurements from [11].

1.1 Outline of Thesis

The structure of the thesis is as follows. Chapter 2 introduces the fundamental theory and concepts of relevant areas for the thesis, including wireless communication channels, electromagnetic wave propagation, reconfigurable intelligent surfaces, ray tracing for wireless channel modeling, and the NVIDIA OptiX framework. In Chapter 3, we explain the working principle of the AIT Ray Tracer, propose an approach for the integration of RISs into the Ray Tracer, and derive our path loss model. Chapter 4 presents the simulation setup for testing and verification of our implementation, and Chapter 5 evaluates the obtained results. Finally, Chapter 6 concludes the thesis by summarizing our findings and providing an outlook on potential extensions enabled by our work.

1.2 Notation

Throughout this thesis, the notation specified in Table 1.1 is used unless otherwise specified.

Table 1.1: Notation used throughout the thesis.

Symbol	Description
$f(.)$	function of a continuous variable
a	scalar
$\underline{\boldsymbol{A}}$	column vector
$\underline{\underline{\boldsymbol{A}}}$	matrix
j	$\sqrt{-1}$
ϕ	azimuth measured from the x-axis of the local coordinate system
θ	elevation measured from the z-axis of the local coordinate system
(x, y, z)	column vector in Cartesian coordinates
(r, ϕ, θ)	column vector in spherical coordinates
$\lvert a \rvert$	absolute value of a
$\lvert\lvert \underline{\boldsymbol{A}} \rvert\rvert_2$	L^2 norm of $\underline{\boldsymbol{A}}$
$\langle \underline{\boldsymbol{A}}, \underline{\boldsymbol{B}} \rangle$	inner product of $\underline{\boldsymbol{A}}$ and $\underline{\boldsymbol{B}}$

Chapter 2

Technical Background

This Chapter introduces the underlying theory and concepts required for the modeling and simulation of reconfigurable intelligent surfaces using ray tracing. An explanation of the wireless communication channels, antenna characteristics, and propagation phenomena is provided to establish a fundamental understanding of electromagnetic wave propagation. Thereafter, the working principle and propagation analysis of the reconfigurable intelligent surfaces are presented. Finally, we discuss ray tracing algorithms for wireless communication and the NVIDIA OptiX engine.

2.1 Electromagnetic Wave Propagation

A wireless communication system consists of a transmitter (Tx), receiver (Rx), and propagation channel. The Tx generates an electric signal that is converted by an antenna into a propagating electromagnetic wave. The wireless propagation channel is the environment through which the wave travels between the two antennas. There typically exist a large number of different propagation paths through which waves can travel. There may be a direct line-of-sight (LOS) connection between the Tx and Rx, but the signal can also interact with other objects in the environment and reach the Rx through reflection, diffraction, or scattering on interacting objects (IOs), as shown in Figure 2.1. Each multi-path component (MPC) has a distinct amplitude, delay, direction of departure from the Tx, and direction of arrival at the Rx. The interference of MPCs can be constructive or destructive depending on the phases of the components as they arrive at the Rx, greatly affecting the received signal strength [7].

Transmitted signals are converted to electromagnetic waves using antennas, likewise, antennas convert electromagnetic waves into received signals. As the antennas interface the Tx and Rx, they are part of the wireless system. Section 2.1.1 will therefore introduce some fundamental antenna characteristics and their impact on the system behavior. To understand the effects of the wireless channel on the received signal, it is necessary to understand the different propagation phenomena. Sections 2.1.2 to 2.1.5 thus provide an introduction to electromagnetic propagation mechanisms.

2.1.1 Antenna Characteristics

The purpose of an antenna is to act as a converter between electromagnetic waves and electric current. Antennas can be defined based on several characteristics and parameters.

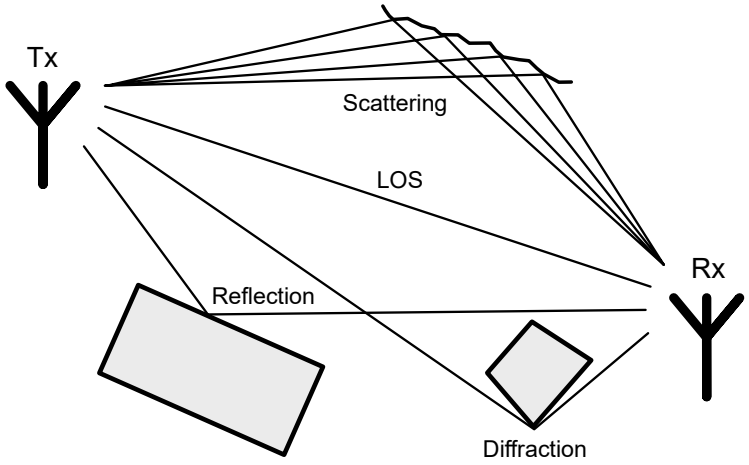

Figure 2.1: Multipath propagation environment with line of sight, reflection, diffraction, and scattering from a rough surface.

Only those required to understand the modeling of antennas in the AIT Ray Tracer will be discussed here.

The most important parameter for the modeling of antennas is the *radiation pattern*, that is, the directional variation in the radiation intensity. Isotropic radiation patterns radiate equally in all directions, whereas directional patterns predominantly radiate in one specific direction [12].

According to the laws of energy conservation, as described in [7], the energy emitted by the antenna must be proportional to the transmitted power P_t. If the Tx antenna radiates isotropically, the power density S at a distance d from the antenna is given by

$$S = \frac{P_\mathrm{t}}{4\pi d^2}\,. \tag{2.1}$$

The Rx antenna has an effective area A_r that describes the antenna's capability to collect the power of the impinging wave. The power received by the Rx is thus

$$P_\mathrm{r} = \frac{P_\mathrm{t}}{4\pi d^2} A_\mathrm{r} \tag{2.2}$$

for isotropic antennas. For non-isotropic Tx antennas, the energy density must be multiplied by the antenna gain $G_\mathrm{t}(\phi_\mathrm{t}, \theta_\mathrm{t})$

$$P_\mathrm{r} = \frac{P_\mathrm{t}}{4\pi d^2} A_\mathrm{r} G_\mathrm{t}(\phi_\mathrm{t}, \theta_\mathrm{t}) \tag{2.3}$$

where $(\phi_\mathrm{t}, \theta_\mathrm{t})$ represents the direction towards the Rx in relation to the transmitter's local coordinate system, i.e., the Tx antenna orientation. Throughout this thesis, the azimuth ϕ is measured from the x-axis of the considered coordinate system, and the elevation θ from the z-axis.

The effective area A_r is proportional to the Rx antenna gain $G_\mathrm{r}(\phi, \theta)$ according to

$$A_\mathrm{r} = \frac{\lambda^2}{4\pi} G_\mathrm{r}(\phi_\mathrm{r}, \theta_\mathrm{r}) \tag{2.4}$$

where λ is the wavelength of the signal, and $(\phi_\mathrm{r}, \theta_\mathrm{r})$ is the direction of the incoming wave in relation to the Rx antenna orientation. By combining (2.3) and (2.4), an expression for the received power P_r is obtained as a function of distance d in free space:

$$P_\mathrm{r} = P_\mathrm{t} G_\mathrm{t}(\phi_\mathrm{t}, \theta_\mathrm{t}) G_\mathrm{r}(\phi_\mathrm{r}, \theta_\mathrm{r}) \left(\frac{\lambda}{4\pi d}\right)^2 \tag{2.5}$$

Equation (2.5) is also known as *Friis' law* and $\left(\frac{\lambda}{4\pi d}\right)^2$ is known as the *free space loss factor*. However, the validity of (2.5) is restricted to the far field, meaning that the two antennas must be at least one *Rayleigh distance* d_r

$$d_\mathrm{r} = \frac{2D^2}{\lambda} \tag{2.6}$$

apart, where D is the largest dimension of either antenna.

Additionally, emitted waves are polarized according to the polarization of the Tx antenna. Likewise, the polarization of the wave must match the polarization of the Rx antenna to avoid negatively impacting the received signal strength [12].

2.1.2 Free Space Propagation

In the simplest scenario, there exists only the LOS and the wave travels directly from the Tx to the Rx without interacting with other objects. Thus, the signal propagates in free space and attenuates with traveled distance. The complex electric field at the receiver is then

$$\underline{\boldsymbol{E}}_\mathrm{LOS} = \frac{\lambda}{4\pi d} \cdot \underline{\boldsymbol{g}}_\mathrm{t}(\phi_\mathrm{t}, \theta_\mathrm{t}) \cdot \underline{\boldsymbol{g}}_\mathrm{r}(\phi_\mathrm{r}, \theta_\mathrm{r}) \cdot \underline{\boldsymbol{E}}_0 \cdot e^{\frac{-j2\pi d}{\lambda}} \tag{2.7}$$

where the emitted electric field $\underline{\boldsymbol{E}}_0$ is a three-dimensional complex vector normal to the wavefront, which considers the magnitude and polarization of the field. The distance d is measured between the Tx and Rx, $e^{\frac{-j2\pi d}{\lambda}}$ is the phase alteration from propagation, and $\underline{\boldsymbol{g}}_\mathrm{t}$ and $\underline{\boldsymbol{g}}_\mathrm{r}$ are complex vectors accounting for the Tx and Rx antenna polarizations and gains in the direction of the wave propagation relative to the antenna orientations [13]. The free space loss factor is $\frac{\lambda}{4\pi d}$ due to the square relationship between the electric field $\underline{\boldsymbol{E}}$ and the directional power density $\underline{\boldsymbol{S}}$, also known as the Poynting vector,

$$\underline{\boldsymbol{S}} = \frac{|\underline{\boldsymbol{E}}|^2}{2\eta_0} \tag{2.8}$$

where $\eta_0 = 120\pi\Omega$ is the impedance of free space [14].

2.1.3 Reflection and Transmission

Reflection and transmission occur when waves propagating through a medium impinge on another medium with different electrical properties. Part of the energy is then reflected back to the first medium, whereas part of the energy is transmitted to the second medium, as shown in Figure 2.2. Specular reflection occurs when the wavelength is significantly *smaller* than the dimension of the object upon which the wave impinges and significantly *larger* than the surface roughness [13]. The surface then reflects according to Snell's law as follows:

$$\theta_\mathrm{r} = \theta_\mathrm{e} \tag{2.9}$$

That is, the angle of incidence θ_e (*Einfallswinkel* in German) is the same as the reflected angle θ_r, whereas the angle of the transmitted wave is given by

$$\frac{\sin\theta_\mathrm{t}}{\sin\theta_\mathrm{e}} = \frac{\sqrt{\delta_1}}{\sqrt{\delta_2}} \tag{2.10}$$

where δ_1 and δ_2 are the complex dielectric constants of the two materials, defined as

$$\delta = \varepsilon - j\frac{\sigma_e}{2\pi f_c} \tag{2.11}$$

where ε and σ_e are the dielectric constant and conductivity of the material, respectively, and f_c, is the carrier frequency of the signal [7].

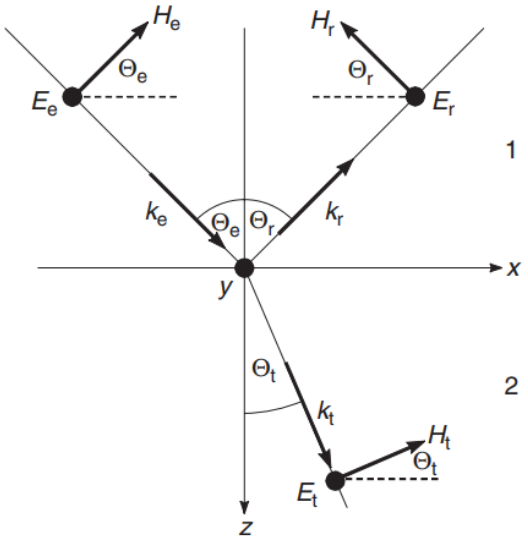

Figure 2.2: Illustration of reflection and transmission mechanisms of an electromagnetic plane wave between media 1 and 2 [7]. The electric field vectors point into the page.

A wave that reaches the Rx after one reflection will yield the complex electric field

$$\underline{\boldsymbol{E}}_{\text{ref}} = \frac{\lambda}{4\pi(d_1+d_2)} \cdot \underline{\boldsymbol{g}}_{\text{t}}(\theta_{\text{t}}, \phi_{\text{t}}) \cdot \underline{\underline{\boldsymbol{R}}} \cdot \underline{\boldsymbol{g}}_{\text{r}}(\theta_{\text{r}}, \phi_{\text{r}}) \cdot \underline{\boldsymbol{E}}_0 \cdot e^{\frac{-j2\pi(d_1+d_2)}{\lambda}} \tag{2.12}$$

where d_1 is the length of the path from the Tx to the reflection point, and d_2 is the length of the path from the reflection point to the Rx. The energy of the reflected wave is accounted for by the Fresnel dyadic reflection coefficient $\underline{\underline{\boldsymbol{R}}}$, which is a 3×3 matrix defined in [13] based on the angle of incidence and material properties.

2.1.4 Diffraction

According to Huygens' principle, each point of a wavefront can be considered the source of a spherical wave. For homogeneous plane waves, the superposition of spherical waves results in another homogeneous plane wave. If parts of the point sources are disrupted by a blocking object, such as a screen or wedge, the blocked point sources with their corresponding spherical waves are eliminated. As shown in Figure 2.3a, constructive and destructive interferences occur in different directions, resulting in a wavefront that is no longer a plane [7].

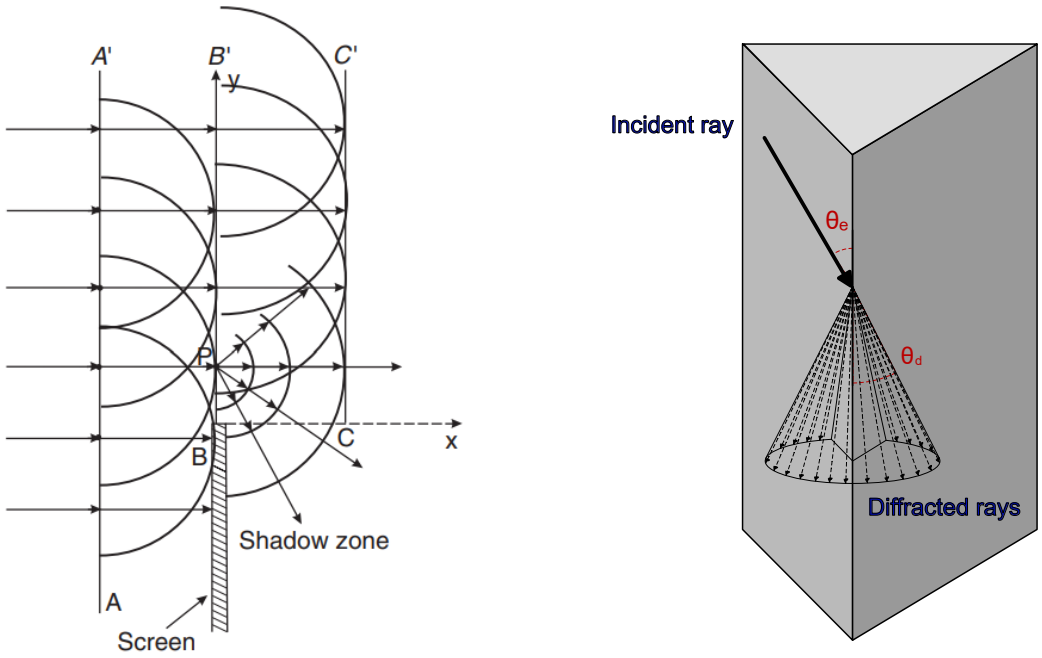

(a) Illustration of Huygens' principle [7].

(b) Illustration of the UTD.

Figure 2.3: A screen or wedge disrupts parts of the point sources, disrupting the planar wavefront as a result.

The electric field of a diffracted wave at the receiver is given by

$$\underline{\boldsymbol{E}}_{\text{diff}} = \frac{\lambda}{4\pi(d_1+d_2)} \cdot \underline{\boldsymbol{g}}_{\text{t}}(\theta_{\text{t}},\phi_{\text{t}}) \cdot \underline{\underline{\boldsymbol{D}}} \cdot \underline{\boldsymbol{g}}_{\text{r}}(\theta_{\text{r}},\phi_{\text{r}}) \cdot \underline{\boldsymbol{E}}_0 \cdot \sqrt{\frac{d_1+d_2}{d_1 d_2}} \cdot e^{\frac{-j2\pi(d_1+d_2)}{\lambda}} \tag{2.13}$$

where d_1 is the length of the path from the Tx to the diffraction point, and d_2 is the length of the path from the diffraction point to the Rx. The energy of the diffracted wave is modeled by the uniform theory of diffraction (UTD), giving the UTD dyadic diffraction coefficient $\underline{\underline{\boldsymbol{D}}}$, a 3×3 matrix defined in [13]. The UTD allows for accurate diffraction calculation for wedges, by modeling diffracted rays as a cone, as shown in Figure 2.3b.

2.1.5 Diffuse Scattering

As mentioned in Section 2.1.3, impinging waves on smooth surfaces are specularly reflected, i.e., the impinging wave reflects in a single direction according to (2.9). Impinging waves on rough surfaces, however, scatter in multiple directions, as illustrated in Figure 2.4. Rough surfaces are defined according to the Rayleigh criterion

$$\Delta h > \frac{\lambda}{8\cos\theta_{\text{e}}} \tag{2.14}$$

where Δh is the height of the roughness and θ_{e} is the angle of incidence [13]. Diffuse scattering in wireless communication, for instance, involves scattering from building facades. There exist several scattering models that determine the strength of the specular and diffuse reflection coefficients. Additionally, the directional characteristics of diffuse reflection can be computed according to the different models presented in [7] and [13].

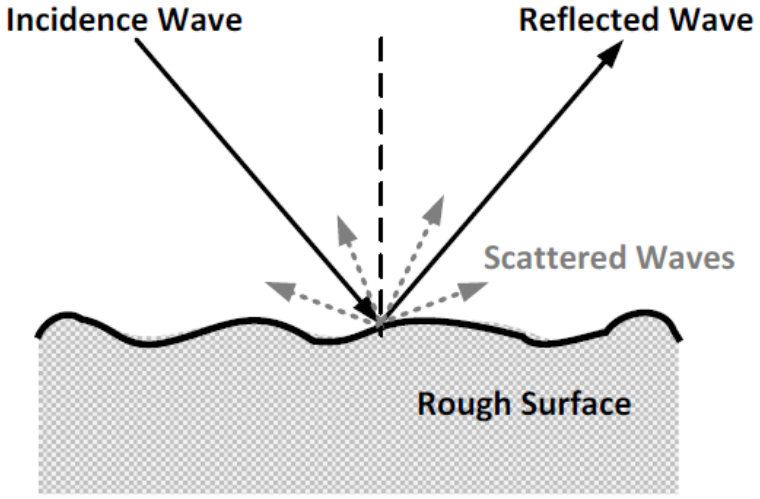

Figure 2.4: Scattering on rough surfaces [13].

2.2 Reconfigurable Intelligent Surfaces

As previously discussed, wireless communication channels are traditionally viewed as uncontrollable: as the signal propagates through the environment and interacts with surrounding objects, it attenuates. Furthermore, propagation hinders the synchronous arrival of signal components, and reflections may cause uncontrollable interference. RISs aim to overcome such unpredictable negative effects by allowing the network to adapt to the environment [5].

RISs are electronically controlled surfaces that adapt their electromagnetic properties, thereby creating unique communication capabilities. With the exception of the control unit, no additional power supply is required to operate an RIS. However, research has shown that active implementations can outperform passive implementations under the same power budget [15]. RISs can be constructed in several ways, including arrays of reflective patch elements, liquid crystal surfaces, and software-defined metasurfaces [5]. This thesis focuses on the first implementation shown in Figure 2.5, i.e., arrays of small subwavelength patch elements, each element with real-time adjustable electromagnetic responses.

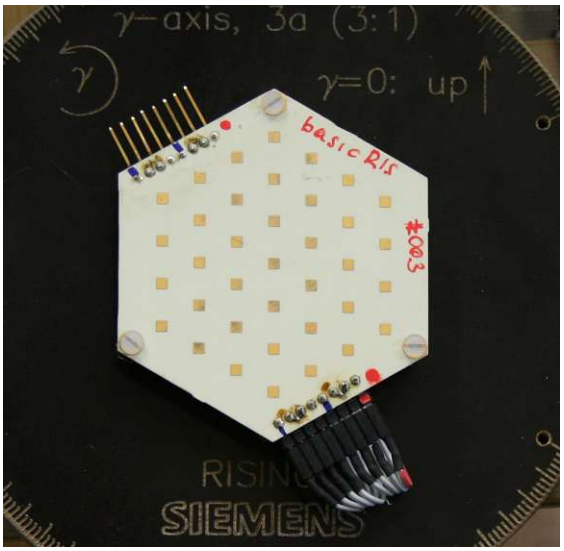

Figure 2.5: An active RIS with 37 patch antenna elements organized in a hexagonal grid. Each element has a real-time adjustable reflection coefficient that can apply an amplification and phase shift to the reflected wave [11].

Each patch element is a small antenna that receives and re-radiates the manipulated signal component. By adding an appropriate delay to the signal, the superposition of all scattered signal components can arrive synchronously at the Rx, causing constructive interference which improves the signal strength. Delayed re-radiation is equivalent to applying a phase shift to a signal. Other ways to manipulate the signal include amplification, frequency adjustment, and polarization [4]. The focus of this thesis is on

RIS elements with controllable amplitudes and phase shifts.

The propagation analysis of an RIS may be reduced to a few steps [4]. First, the emitted wave from the Tx must be computed. The impinging wave at each RIS element can be determined based on the free space path loss and antenna characteristics of the individual elements. Thereafter, the radiated field from each RIS element is computed, and the superposition of the radiated waves yields the electric field at the Rx. Due to great research interest, several RIS path loss models have been developed in recent years. [16] provides an overview of many of the recent models with their main features and limitations. For improved flexibility and compatibility with the AIT Ray Tracer, we compartmentalized and adapted the experimentally verified path loss model from [10] for this thesis. The adapted model enables the simulation of more complex scenarios, for instance by allowing reflections to and from the RIS and removing the dependency on a directive antenna model for the Tx and Rx.

2.3 Ray Tracing

The concept of ray tracing originates from the field of computer graphics. Originally, the motive was to find ways to create photorealistic images, i.e., computer-fabricated images that resemble photos. The idea emerged as researchers in computer graphics observed physicists designing lenses by plotting paths taken by rays of light, starting from the light source and passing through the lens. It was thus discovered that simulation of light physics could be a good approach for creating synthetic images [17].

For graphical applications, ray tracing aims to determine the color of every pixel on a screen. This is obtained by averaging the color of the rays that reach the viewer behind the screen. The working principle of ray tracing in graphics is illustrated in Figure 2.6. In reality, a light source in a scene will emit photons. The photons travel through space and interact with the environment: they may reflect on or be absorbed by surrounding objects. Every photon that reaches the viewer's eye will be visible as the color corresponding to its frequency after interaction with the environment. Similarly, in graphical ray tracing, rays of a certain color leave the light source and propagate through the scene. The color and intensity of the ray update according to the objects it interacts with. Only rays that pass through the screen and reach the viewer will contribute to the actual image. The color of each pixel will thus be the average color of all the received rays within the bounds of the pixel [17].

In literature, the term *ray tracing* may be used to describe different concepts. The expression sometimes refers to ray approximation in the general sense, other times it refers to a specific implementation method or the identification of intersection points between a 3D line and a set of 3D objects.

2.3.1 Rays in Electromagnetic Wave Propagation

Rays used for modeling wireless communication channels are equivalent to those of visible light. The same ideas used in graphics can thus be employed for wireless channel

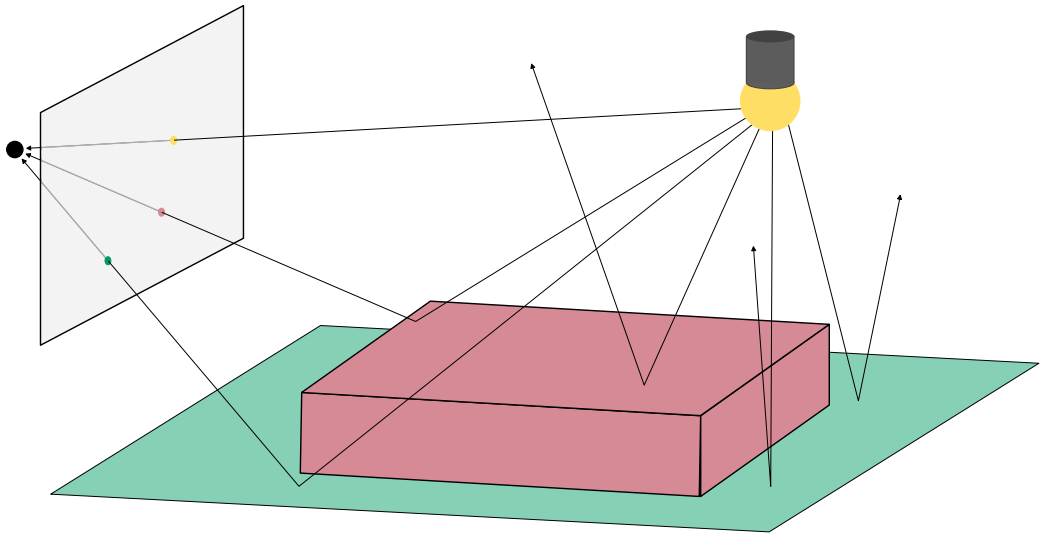

Figure 2.6: Working principle of the forward ray tracing algorithm for computer graphics. Rays that mimic photons are emitted from the light source and propagate through the environment. Only rays that reach the viewer through the screen are accounted for in the rendered picture. The color of a ray is determined by its interactions with the environment.

modeling, in fact, ray tracing has been used in the field since the 90s [7]. The concepts of rays and geometrical optics can be justified using the high-frequency approximation of Maxwell's equations as rigorously described in [18], also summarized in [8]. High-frequency approximation means that the wavelength of the electromagnetic wave, in relation to the structures with which the wave interacts, is so small that the wavefront can be approximated as a plane wave, and therefore modeled as a ray traveling in the direction of the surface normal. Through the derivations seen in [18, 8], one can show Fermat's principle of least time, which states that a ray that travels between two points in space will take the path that requires the minimum traveling time. From Fermat's principle, it is possible to derive the laws of reflection, transmission, and diffraction. Electromagnetic rays are perpendicular to the wavefronts and travel in a straight path through homogeneous media, obey the laws of reflection, refraction, and diffraction, and carry energy.

2.3.2 Ray Tracing Algorithms

An essential part of ray tracing is establishing the paths between a source and a target, such as a light source and the viewer's eye in computer graphics, or two antennas in radio channel modeling. Determining valid paths between the two points is not trivial, but has been a big research topic over the past decades. The two most popular algorithms for

ray tracing for channel modeling are the *shooting and bouncing ray (SBR) method* and the *image method*. The SBR method is also known as *ray launching* as rays are launched from the Tx to determine if they arrive at the Rx. Likewise, the image method is often referred to as *ray tracing* as it traces rays from the Rx back to the Tx. Additionally, there exist *hybrid methods* that combine ideas from both the SBR method and the image method. In this Section, the three methods will be introduced and discussed.

Shooting and Bouncing Ray Method

The shooting and bouncing ray method was originally introduced in [19] to determine the internal radar cross-section of a cavity, and has been frequently used in radio channel modeling since then [8]. The general idea is to launch a large number of uniformly distributed rays from the Tx, as shown in Figure 2.7a. Rays propagate through the scene until they hit an object, causing new rays to spawn according to the propagation mechanisms described in Section 2.1 [7, 8]. Generally, the Rx is modeled as a sphere to capture rays that contribute to the signal at the Rx. The accuracy of the ray trajectories may therefore not be ideal. For reliable results, proper selection of reception sphere radius and sampling rate of the unit sphere around the Tx are thus essential [9]. Rays that become too attenuated to be significant, i.e., drop below the noise floor, are terminated.

A great challenge with the SBR method is the reduced granularity of rays as the traveled distance from the Tx increases. As rays propagate further from the Tx, the distance between adjacent rays increases, potentially missing the reception sphere, as shown in Figure 2.7b. To maintain high accuracy, *ray splitting* may be employed, in which case rays that have propagated a certain distance from the Tx are subdivided into multiple new rays with recomputed energy distribution [7]. A 2D example of this is seen in Figure 2.7c.

Although the SBR method can produce good results, the computational complexity quickly increases with a higher sampling rate, in particular when considering diffraction and diffuse scattering, as this requires spawning of an extremely large number of rays.

Image Method

The image method computes valid reflection paths between the antennas by tracing the *images* of the Rx with respect to the surfaces in the environment. In fact, a reflected ray on a surface follows the same trajectory as if the ray was launched from the image of the Rx with respect to the reflection surface, as seen in Figure 2.8. A reflection point can thus be identified by locating $\underline{\boldsymbol{R}}'$, the surface image of the Rx, and connecting it with the Tx. The reflection point $\underline{\boldsymbol{P}}$ is the point of intersection between the line segment and the plane representing the surface, and the reflected path is the direct path between the Tx, the reflection point, and the Rx [8].

To locate every valid reflection path in an environment, the image method must be performed on every existing surface. Second-order reflections are determined by computing the image of $\underline{\boldsymbol{R}}'$ with respect to every other surface in the scenario, as seen in Figure 2.9. This can be extended to higher-order reflections by considering every permutation of

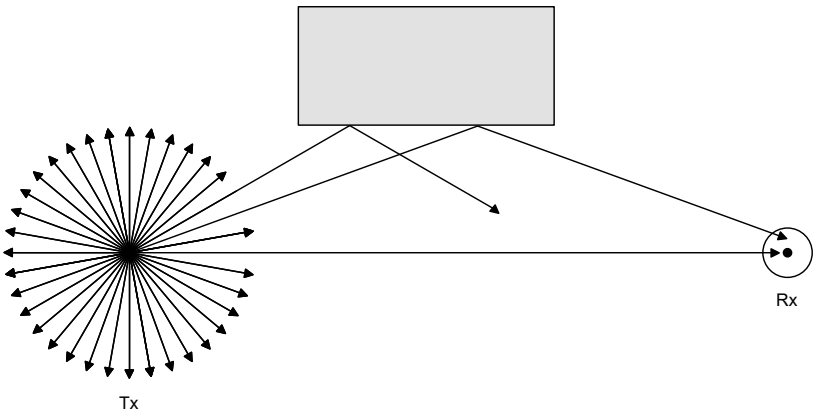

(a) Shooting and bouncing ray method.

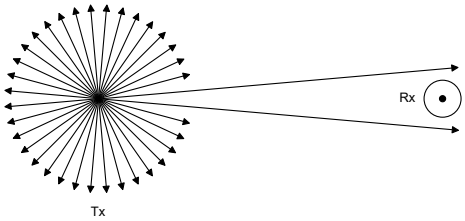

(b) Missed reception sphere.

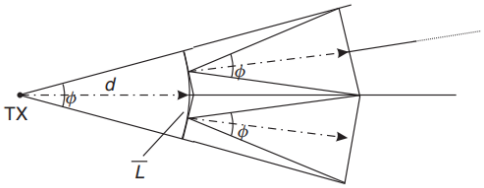

(c) Ray-splitting algorithm [7].

Figure 2.7: Examples of the shooting and bouncing ray method and the ray-splitting algorithm.

surfaces for every considered order. Evidently, the computational complexity increases exponentially for each considered reflection order, thus often becoming infeasible even when simplifying the geometry or pruning the reflection tree [20]. An additional challenge is the implementation of diffraction and diffuse scattering, as they are non-trivial [7].

Hybrid Methods

Due to the limitations of the two methods, hybrid methods have been proposed to take advantage of the fast computation speed of SBR and the accuracy of the image method. In [21], the SBR method was employed to find valid paths. Thereafter, the image method was applied only for the identified permutations to find the precise paths and reflection points. In [9], potential reflection, diffraction, and diffuse scatter points were obtained analytically using cheaper algorithms without rigorous validity checks. Rays were thereafter launched toward the analytically determined points, ensuring that only non-blocked rays arrive at the Rx.

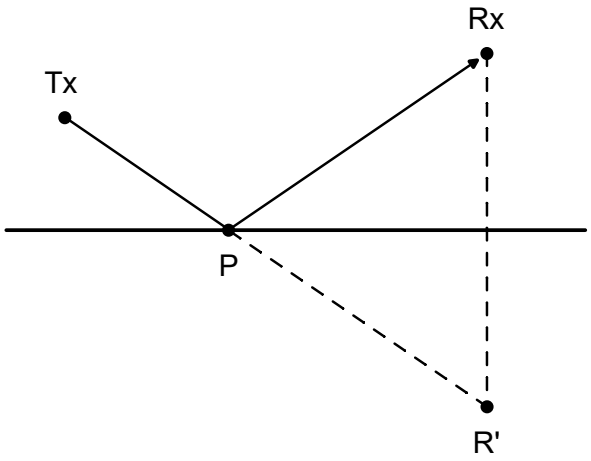

Figure 2.8: Identifying a first-order reflection through the image method.

2.3.3 GPU Acceleration

Different acceleration methods may be employed to improve the computational efficiency of ray tracing, such as space division methods or 2D simplifications. An increasingly popular approach is the use of GPUs due to their ability to exploit a very high degree of parallelism [8]. The essential difference between central processing units (CPUs) and GPUs is the number of cores per chip. CPUs typically have a small number of powerful general-purpose cores whereas GPUs have a much larger number of simpler and slower cores, as illustrated in Figure 2.10. Although GPUs primarily are used for gaming and graphics, the hardware is perfect for performing a large number of simpler computations in parallel. In later years, GPUs have therefore become more common in general-purpose computing as well [22]. To benefit from GPUs, it is of high importance that the code can be massively parallelized, as the individual GPU cores are significantly slower than CPU cores. Code that frequently requires a lot of synchronization and data exchange may therefore not achieve the anticipated speedup. Often in ray tracing, a very large number of rays are launched, propagating and interacting with the environment independently from one another. By utilizing GPUs, the rays can be distributed over thousands of threads and processed in parallel, thus significantly improving the overall run-time.

2.4 NVIDIA OptiX

Utilizing the full potential of GPUs is a great challenge, despite the inherent parallelizability of ray tracing algorithms. The NVIDIA OptiX ray tracing engine is designed to overcome the major bottlenecks for GPU-accelerated ray tracing by providing a flexible and efficient framework. To support a wide range of ray tracing implementations, OptiX is built as a general, low-level ray tracing engine, focusing on the fundamental computations, i.e.,

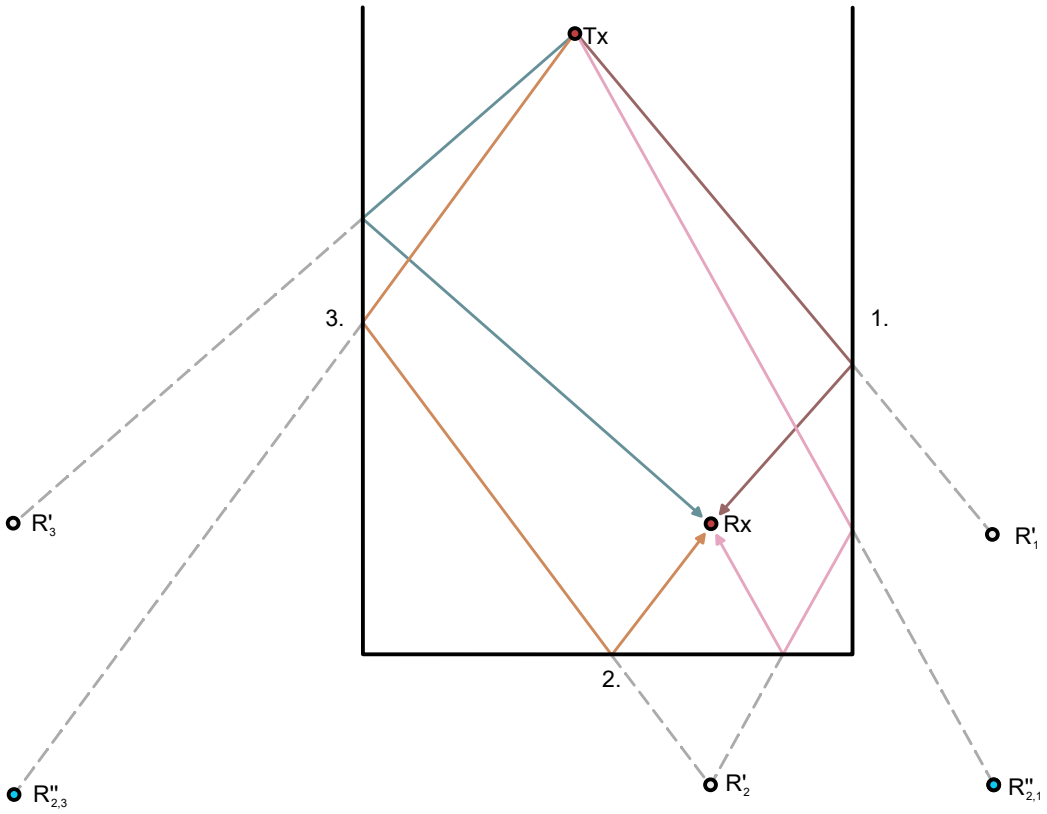

Figure 2.9: Identifying higher-order reflections through the image method. In this example, first-order reflections are identified for surfaces $\{1\}$ and $\{3\}$, and second-order reflections are identified for surface permutations $\{2, 3\}$ and $\{2, 1\}$. Note that for a complete first- and second-order image method, all permutations must be considered.

computing the intersection points between a 3D line and a set of 3D objects. There exist no built-in concepts of light, shadows, reflection, or any other optical phenomena. Instead, the user writes their own programs to generate rays and define the response of rays as they hit objects, offering great flexibility and potential for applications across several fields [23].

2.4.1 System Overview

The OptiX engine consists of two APIs:

a) A host-based API consisting of C functions that can be called from the CPU to perform the preparation of the GPU for ray tracing. This includes setting up the context (the instance running the OptiX engine), defining the environment (creating geometries

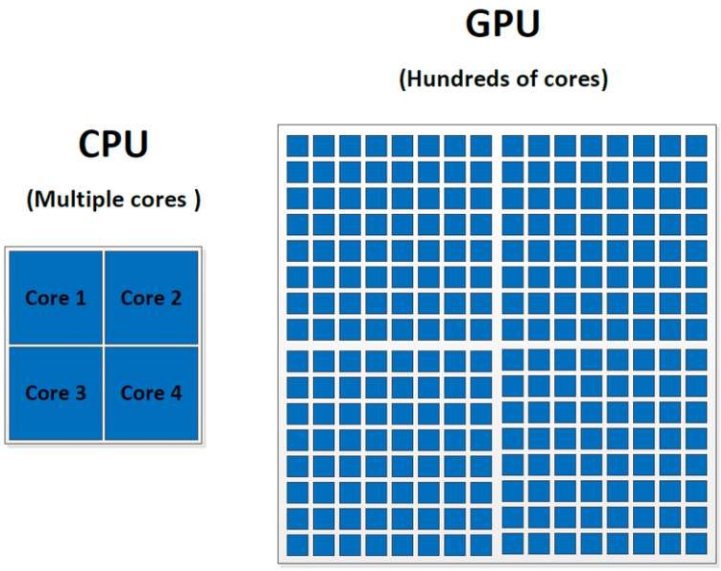

Figure 2.10: Cores in a CPU (left) and a GPU (right) [22].

and other data structures used for the ray tracing), and launching the ray tracing kernels.

b) A CUDA C++ device-based program API that can be called from the GPU during the execution of kernels. This includes function calls for generating and tracing rays, accessing data, and reporting and responding to intersections.

The generation and behavior of the rays are defined by the user through *programs* that are executed during the ray tracing. Prior to ray tracing, the application must perform the setup by making function calls from the host API. This includes setting up the scene, linking the different user-defined programs to the correct geometry instances, and preparing buffers. When the preparation and setup are complete, the application executes the ray tracing kernel by launching the context. The launching invokes the user-defined ray generation program, in which rays are created, prepared, and traced. Intersections of rays and objects are detected according to the user-defined intersection programs for the corresponding geometry. The behavior of the rays as they intersect geometries in the scene and not, is determined by user-defined hit and miss programs, respectively. The call graph for the ray tracing kernel is demonstrated in Figure 2.11.

Objects in the scene are defined by *geometries* and *materials*. Each geometry instance consists of a geometry object and a material object. The geometry object contains a list of geometric primitives associated with a bounding box program and an intersection program (see Section 2.4.2). This defines the geometric properties of the object and therefore determines whether launched rays will hit the object or not. The material is associated with hit programs, thus determining the behavior of rays that hit the geometry instance. Additionally, the user can define *ray types* which allow multiple types of ray

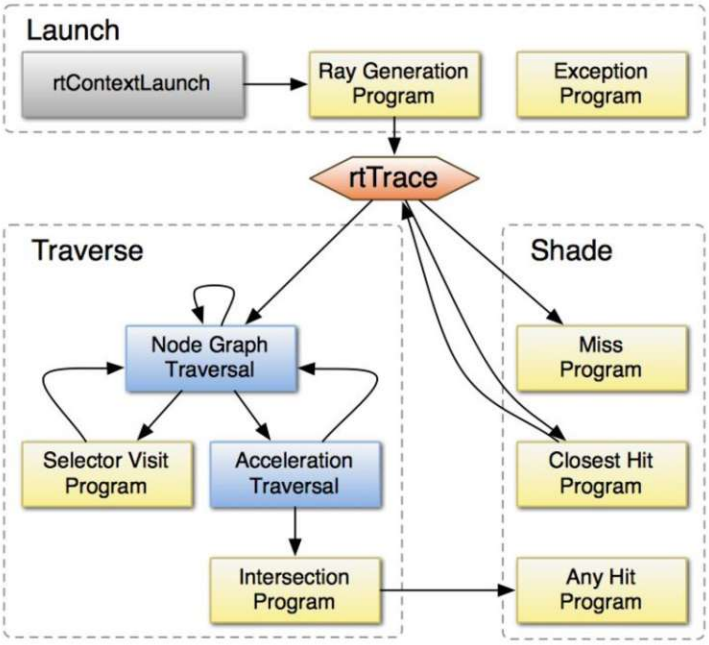

Figure 2.11: A call graph for the OptiX ray tracing pipeline. Yellow boxes represent user-defined programs, and blue boxes represent internal algorithms. The execution is initiated by calling `rtContextLaunch` from the host API. This triggers the ray generation program, from which rays can be created, prepared, and finally traced by calling `rtTrace` [23].

tracing operations to be executed on the same geometry instance. This may for instance be used to distinguish between rays that implement different optical phenomena.

2.4.2 Programs

This section provides an overview of the most important OptiX programs responsible for defining the generation and behavior of rays. Each program operates independently on a single ray at a time according to the ray tracing pipeline in Figure 2.11. The operation `rtTrace` alternates between locating intersections (*Traverse*) and responding to them (*Shade*).

Ray Generation

Each launched thread executes the ray generation program. The program creates one or multiple rays, prepares, and launches them. The preparation includes specifying the origin of the ray in the scene, the direction toward which the ray is launched, the ray type, and, optionally, buffers containing any additional data.

Geometry Programs

Two of the important geometry programs are intersection programs and bounding box programs. These correspond to the scene traversal and are used to identify intersection points. Intersection programs are defined for each geometry and implement intersection tests to determine if a ray intersects the geometric object. Additionally, intersection programs may compute attributes of the intersection based on the hit position, such as the surface normal.

Bounding box programs are applied to each geometry and define boxes as coarse bounds containing one or multiple geometries. As intersection tests are the most expensive tasks in a ray tracer and are repeated several times, bounding box programs are used to enable acceleration by quickly assisting in deciding which objects from a scene may intersect with a ray or not, reducing the number of required intersection checks.

Material Programs

The material programs determine how a ray behaves as it intersects an object of said material. There exist closest-hit and any-hit programs. A closest-hit program is called as soon as the ray's nearest intersection point has been identified, whereas any-hit programs are called during traversal for every intersection point between the ray and scene. Hit programs may for instance terminate, relaunch, or manipulate the ray, and are therefore the programs where reflections and other optical phenomena can be implemented.

Miss Program

Miss programs are called by rays that don't intersect any object in the scene.

Chapter 3

Implementation

The previous Chapter provided the background required to understand the fundamental workings of reconfigurable intelligent surfaces and wireless communication modeling using ray tracing. In this Chapter, we introduce the AIT Ray Tracer, designed to efficiently and accurately simulate the propagation effects of electromagnetic waves in stationary and non-stationary wireless communication channels. After discussing the implementation and capabilities of the Ray Tracer, we present an approach for the integration of RISs and derive a new path loss model to accurately model RISs in complex environments.

3.1 AIT Ray Tracer

The AIT Ray Tracer is developed in CUDA C++ and uses the NVIDIA OptiX framework to efficiently and accurately simulate the propagation effects of electromagnetic waves in wireless communication channels on GPUs. The Ray Tracer supports both stationary and non-stationary scenarios and employs a hybrid ray tracing method for high performance and accuracy. Rays are thus not launched in all directions from the Tx, but only in the directions of analytically determined reflection, diffraction, and diffuse scatter points that are obtained beforehand using cheaper algorithms without rigorous validity checks. The ray generation program is implemented to mimic the Tx by launching rays with electric fields initialized according to the Tx polarization, gain, and radiation pattern. OptiX traverses the rays and identifies intersection points according to the geometry intersection programs. As rays intersect objects, the corresponding object hit program executes. The material hit programs implement the supported wave phenomena (reflection, diffraction, and diffuse scattering) for every defined material. The received electric field is updated according to the Rx polarization, gain, and radiation pattern for every ray that intersects the Rx geometry instance. Therefore, only non-blocked rays arrive at the Rx, compensating for the potential inaccuracies in the cheaper algorithms employed to determine points toward which rays should be launched.

The AIT Ray Tracer is provided with a configuration file defining the antenna models and ray tracing parameters, and a description of the simulation environment through geometry and material `.csv` files. The Ray Tracer imports the scenario, thereafter, performs the ray tracing, and, for each ray, computes the direction of arrival, complex electric field, and delay. For additional verification of the obtained MPCs, we implemented a path visualization tool in MATLAB.

3.1.1 Modular Architecture

The AIT Ray Tracer consists of two phases:

a) C++ code that predominately is executed sequentially on the CPU and imports the environment and configuration parameters, prepares the context with geometry instances, and computes reflection, diffraction, and diffuse scatter points.

b) CUDA C++ code that implements the OptiX programs described in Section 2.4.2 and is executed in parallel on the GPU according to Figure 2.11.

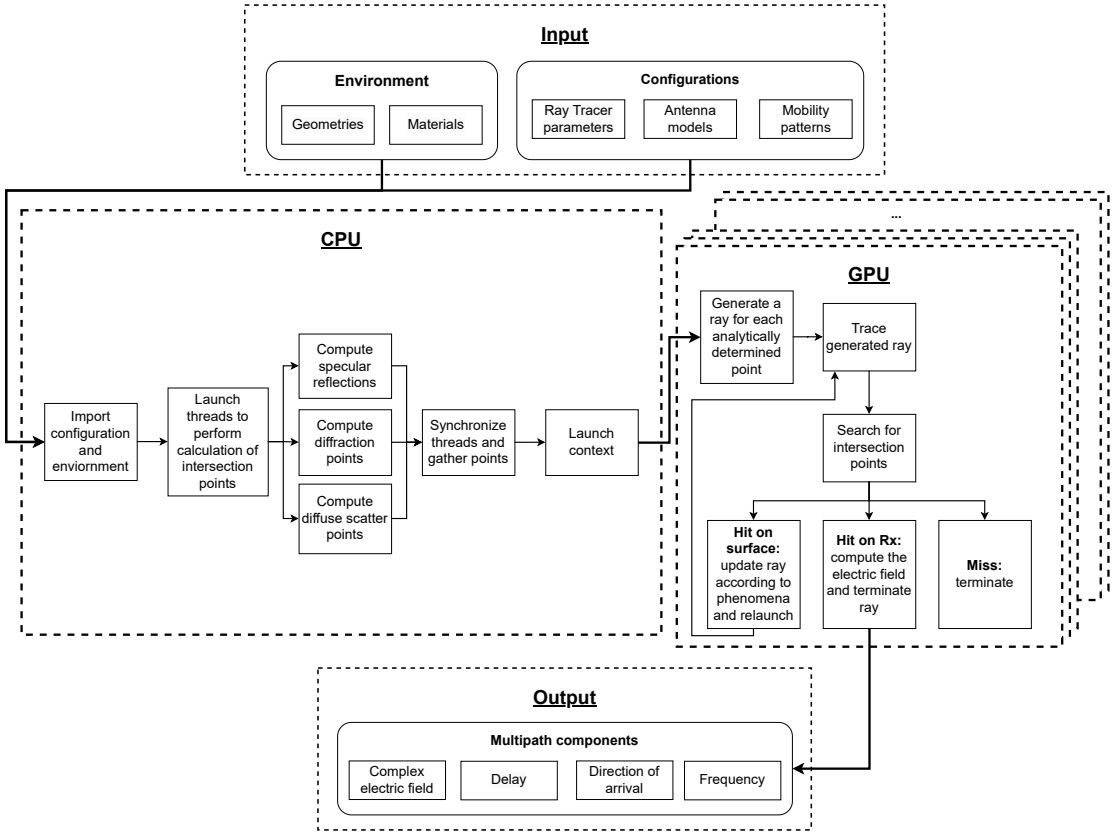

Figure 3.1: Code flow of the AIT Ray Tracer. The Ray Tracer is executed both on the CPU and GPU. The scenario is imported and processed sequentially on the CPU, and points toward which rays should be launched are computed in parallel. The GPU performs the ray generation and tracing using OptiX, with one ray per thread. Results are returned to the CPU and written to `.csv` files.

An overview of the code flow is demonstrated in Figure 3.1. The modular architecture of the Ray Tracer is beneficial as additional features, geometry representations, and antenna patterns can be incorporated without altering the essential functionality of the

Ray Tracer. Input files provide the Ray Tracer with relevant configuration parameters, antenna descriptions, and the wireless channel as geometry and material files which are further described in Section 3.1.2. After the scenario has been imported and processed, points toward which rays should be launched are computed in parallel on CPU threads as described in Section 3.1.3. Ray tracing is executed in parallel by OptiX with one ray per GPU thread. Each ray is generated and initialized according to the Tx characteristics as discussed in Section 3.1.4 and the propagation mechanism it models. For instance, rays corresponding to diffraction points require additional data to compute the diffracted field according to the UTD. Additionally, ray types are used to distinguish between the different phenomena implemented in the material hit programs, ensuring that the direction and electric field of relaunched rays are updated correctly. The complex electric field of rays that intersect the Rx are computed according to the Rx characteristics (described in Section 3.1.4) and written to an output file from the CPU.

The scenario is completely stationary throughout the ray tracing with OptiX. Non-stationary scenarios are supported by performing multiple iterations of stationary ray tracing, in which the antenna positions are updated in discrete steps according to the mobility patterns specified in the input configuration.

3.1.2 Modeling an Environment

As discussed in Section 2.4, scenes in OptiX consist of one or several *geometry instances* composed of a geometry object that defines the geometric properties of the instance and a material object that defines the behavior of rays that intersect the instance. The Ray Tracer, therefore, imports the environment through two `.csv` files: one specifying each geometric object and its corresponding materials, and one specifying the material properties of the implemented materials (concrete, glass, metal, wood, and drywall).

Currently, the only supported geometry format is z-aligned axis geometry (ZAG), where each geometry is a block defined by four (x, y)-coordinates, as in Figure 3.2, with a bottom z-coordinate, top z-coordinate, and material. Simpler scenarios can thus easily be created by hand as in Figure 3.3a, whereas more complex street scenarios as in Figure 3.3b can be converted from OpenStreetMap (OSM) files using available MATLAB scripts.

When geometry objects are imported and processed on the CPU, they are subdivided into six surfaces, allowing more efficient intersection algorithms to be employed. As the only implemented geometry format is ZAG, every surface is assigned the same intersect and bounding box programs. The closest hit programs are assigned according to the material specified in the input file, determining the behavior of rays as they intersect the surface. Every material hit program implements the aforementioned wave phenomena but has different material properties. To distinguish between the different phenomena and treat them accordingly, `ray types` are used. Upon intersection with a surface, each ray applies a phase shift according to the traveled distance and updates the total path length to account for the free space path loss if the ray reaches Rx. Additionally, the electric field and outgoing direction are evaluated according to the ray type, e.g., according to the Fresnel equations for reflected rays. Thereafter, rays are relaunched from the intersection point with updated directions until the Rx is hit, the scene is missed, or

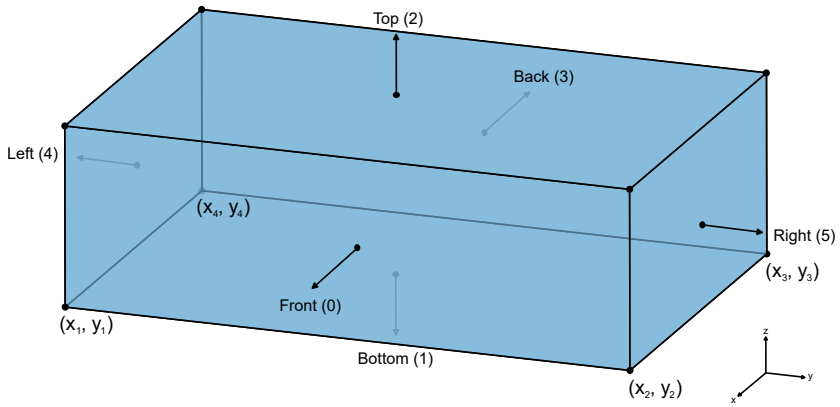

Figure 3.2: Z-aligned axis geometry block defined by four (x, y)-coordinates, a bottom z-coordinate, a top z-coordinate, and a material. The block consists of six numbered faces, as seen in the figure.

the maximum reflection depth is exceeded. For diffracted and scattered rays, there exist certain exceptions for relaunching rays. These are discussed in the following section.

3.1.3 Computation of Paths

This Section describes the process of analytically determining reflection, diffraction, and diffuse scatter points. Reflections are of higher importance than diffractions and scattering in this thesis and will therefore be described in more detail.

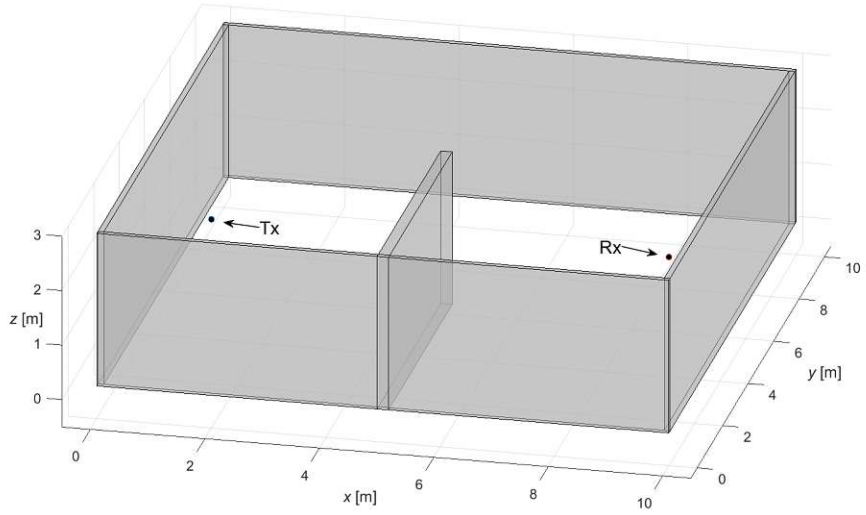

(a) Indoor scenario created manually.

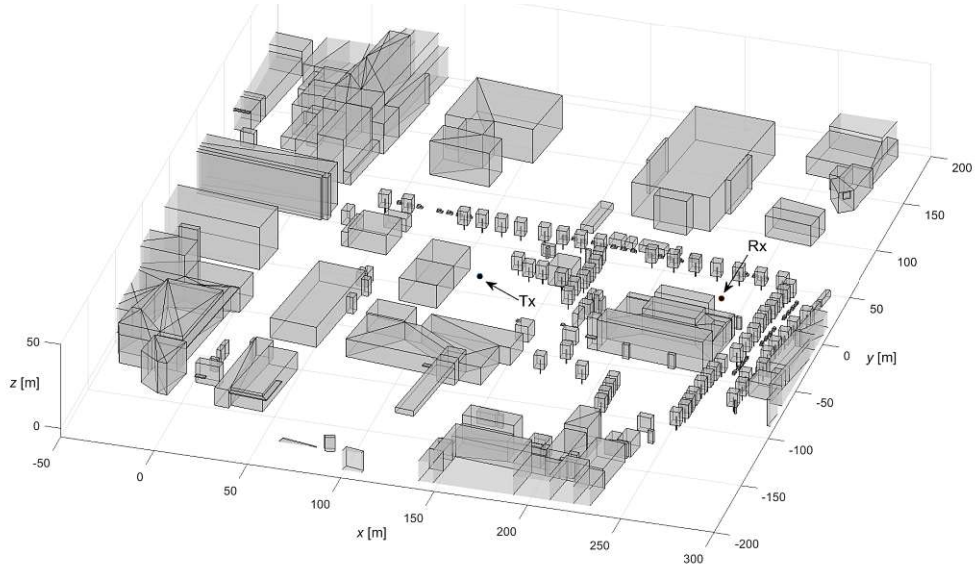

(b) Outdoor scenario converted from OpenStreetMap file.

Figure 3.3: Examples of scenarios that can be modeled with a ZAG format.

Reflection

Reflections up to order $n_{\max}$, including LOS which are considered reflections of zeroth order, are computed according to a simplified image method as described in [9]. The Rx at point $\underline{\boldsymbol{R}} \in \mathbb{R}^3$ is orthogonally projected onto a given sequence of n surfaces. Surfaces are spanned by vectors $\underline{\boldsymbol{u}}, \underline{\boldsymbol{v}} \in \mathbb{R}^3$ with surface normal $\underline{\boldsymbol{n}} = \underline{\boldsymbol{u}} \times \underline{\boldsymbol{v}}$ and an anchor point $\underline{\boldsymbol{a}} \in \mathbb{R}^3$ which is the center point of the surface. The point of the k-th image of the receiver, $\underline{\boldsymbol{P}}_k$, for a given permutation of surfaces, is computed according to (3.1), starting with $\underline{\boldsymbol{P}}_0 = \underline{\boldsymbol{R}}$. The direction of the n-th order reflection point for the given sequence of surfaces is thus the direction from the Tx at point $\underline{\boldsymbol{T}} \in \mathbb{R}^3$ to $\underline{\boldsymbol{P}}_n$, the n-th image of the Rx, i.e., $\frac{\underline{\boldsymbol{P}}_n - \underline{\boldsymbol{T}}}{||\underline{\boldsymbol{P}}_n - \underline{\boldsymbol{T}}||_2}$.

$$\underline{\boldsymbol{P}}_k = -\underline{\boldsymbol{P}}_{k-1} + 2\left[\begin{pmatrix} \underline{\boldsymbol{u}}_k^T & \underline{\boldsymbol{v}}_k^T \end{pmatrix} \frac{1}{1 - \langle \underline{\boldsymbol{u}}_k, \underline{\boldsymbol{v}}_k \rangle^2} \begin{pmatrix} 1 & \langle \underline{\boldsymbol{u}}_k, \underline{\boldsymbol{v}}_k \rangle \\ -\langle \underline{\boldsymbol{v}}_k, \underline{\boldsymbol{u}}_k \rangle & 1 \end{pmatrix} \begin{pmatrix} \langle \underline{\boldsymbol{P}}_{k-1} - \underline{\boldsymbol{a}}_k, \underline{\boldsymbol{u}}_k \rangle \\ \langle \underline{\boldsymbol{P}}_{k-1} - \underline{\boldsymbol{a}}_k, \underline{\boldsymbol{v}}_k \rangle \end{pmatrix} + \underline{\boldsymbol{a}}_k \right] \tag{3.1}$$

To identify every reflection up to order $n_{\max}$, the procedure described above is performed for every valid permutation of surfaces for every order $n \in \mathbb{N} : 0 \leq n \leq n_{\max}$, where valid permutations of surfaces are permutations in which the same surface does not appear twice consecutively. To detect blocked paths between two intersection points, a simple tracing algorithm is used, in which the geometry structures are simplified as axis-aligned bounding boxes.

Diffraction

The Ray Tracer accounts for first-order diffractions by launching rays toward identified diffraction points computed according to the UTD as described in [24]. Edges are detected by locating all adjoining surfaces in the environment, i.e., two surfaces that share two or more vertices. For each adjoining surface pair, the corresponding diffraction point is computed. Using the same simplified tracing algorithm as for reflections, valid diffraction points are identified, i.e., points that have LOS to Tx and Rx. During ray tracing, diffracted rays are relaunched directly toward the Rx with an electric field computed according to the UTD. Unlike the simple algorithm performed to eliminate blocked reflection and diffraction paths on the CPU, the ray tracing on the GPU implements accurate intersection programs. Therefore, every blocked path will be detected, ensuring that only valid diffraction paths are accounted for at the Rx.

Diffuse Scattering

Diffuse scattering can be modeled as a non-uniform spherical wave originating from the center of surface elements [25]. In practice, this is implemented by virtually splitting rough surfaces into smaller surface elements using a tiling algorithm. The Ray Tracer implements the tiling algorithms discussed in [9], and the center point of each tile represents a diffuse scatter point toward which a ray should be launched. For each diffuse intersection, a scattered ray is launched directly toward the Rx with an electric field computed according to the directive diffuse scattering model described in [25]. The directive model assumes that the maximum energy is concentrated toward the specular reflection, with a scattering attenuation coefficient that depends on the angle of the scattered ray in relation to the angle of the specular reflection. The scattered ray is only accounted for at the Rx if the path is unblocked, i.e., if there is LOS between the diffuse intersection point and the Rx. Otherwise, the diffuse scatter ray is specularly reflected until LOS to the Rx is obtained or the maximum number of reflections is exceeded.

Non-Stationary Scenarios

Non-stationary scenarios are simulated by performing ray tracing in multiple stationary steps, starting at the initial position of the antennas, and updating them according to the specified mobility pattern for each stationary step. The changed position between stationary steps impacts the MPCs, therefore, paths must be recomputed for each Tx and Rx position. For improved performance, this is executed in parallel over multiple CPU threads.

3.1.4 Antenna Implementation

The configuration file passed to the Ray Tracer contains information regarding the position, velocity, acceleration, and orientation of the antennas. Additionally, antenna radiation pattern models are selected, and model parameters are specified. Whereas the Rx is defined as a geometry instance with corresponding intersection, bounding box, and hit

programs, the Tx is not defined as a geometric entity. Instead, the Tx implements the ray generation program. This section elaborates on the antenna implementations.

Radiation Patterns

In Section 2.1.1, some important antenna characteristics were presented, including radiation patterns that describe the directional variation in radiation intensity. The signal strength of MPCs may thus highly depend on the outgoing angle from the Tx and the incoming angle to the Rx. Different types of antennas can be modeled by finding suitable models for the normalized field pattern $F(\phi, \theta)$, which is given by

$$F(\phi, \theta) = \frac{E(\phi, \theta)}{E_{\max}} \tag{3.2}$$

where $E_{\max}$ is the maximum value of the magnitude of $E(\phi, \theta)$ over a sphere, with azimuth ϕ and elevation θ [26].

The AIT Ray Tracer implements isotropic and dipole antenna models. Additionally, interpolation of measured data is supported. To simulate the desired scenarios for this thesis, an additional directional cosine antenna model was implemented.

Isotropic Antennas: Isotropic antennas radiate equally in all directions. The normalized field pattern is therefore given by

$$F_{\text{isotropic}}(\phi, \theta) = 1\,. \tag{3.3}$$

Dipole Antennas: Dipole antennas consist of two conductive wire rods. There exist different types of dipole antennas. In the Ray Tracer, finite length dipoles are considered, which have a normalized field pattern

$$F_{\text{dipole}}(\phi, \theta) = \left(\frac{\cos\left(\frac{kl}{2}\cos\theta\right) - \cos\left(\frac{kl}{2}\right)}{\sin\theta} \right)^2 \tag{3.4}$$

where l is the length of the antenna and k is the wave number [27]. An example of (3.4) is plotted in Figure 3.4a.

Directional Antennas: Directional antennas radiate predominantly in one specific direction. This can be modeled by a cosine model

$$F_{\cos}(\phi, \theta) = \begin{cases} (\cos\theta)^k & \text{if } 0 \le \theta \le \frac{\pi}{2} \\ 0 & \text{if } \frac{\pi}{2} \le \theta \end{cases} \tag{3.5}$$

where $k = \frac{G}{2} - 1$ and G is the directional gain of the antenna. Equation (3.5) is plotted in Figures 3.4b and 3.4c for $k = 5$ and $k = 20$.

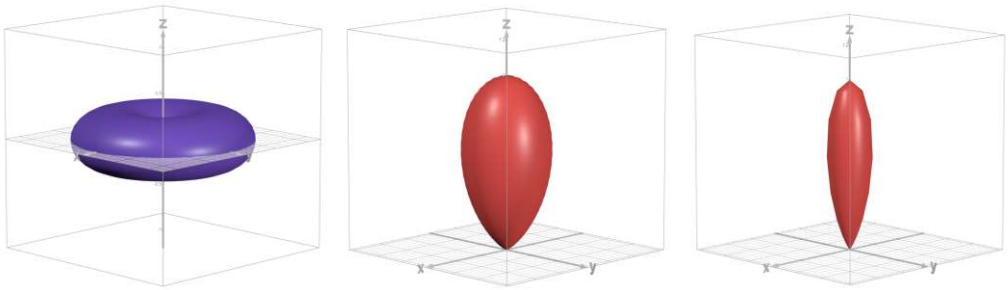

(a) Dipole (b) Directional, $k = 5$ (c) Directional, $k = 20$

Figure 3.4: Normalized radiation patterns in the AIT Ray Tracer.

Transmitter

The ray generation program, called once per executed thread, is implemented to mimic the behavior of the Tx by creating, preparing, and launching rays toward the predetermined intersection points obtained as described in Section 3.1.3. Each generated ray is initialized with an origin, direction, and ray type. The origin is always $\underline{\boldsymbol{T}}$, the position of the Tx, and the ray type corresponds to the phenomena that the ray models. The direction is $\frac{\underline{\boldsymbol{P}}_i - \underline{\boldsymbol{T}}}{\|\underline{\boldsymbol{P}}_i - \underline{\boldsymbol{T}}\|_2}$, i.e., the direction from the Tx to the corresponding intersection point $\underline{\boldsymbol{P}}_i$. Additionally, every launched ray holds a reference to its corresponding *ray data*, a data structure containing all the data required throughout the ray tracing, such as the electric field, delay, total path length, and data related to the propagation mechanism. The complex electric field is initialized according to the Tx polarization, gain, and normalized radiation pattern.

Receiver

As discussed in Section 2.3, a receiver may either be modeled as a point or a reception sphere depending on the ray tracing algorithm, where reception spheres typically are used for SBR methods to additionally capture rays that aren't directly launched toward the Rx. As the AIT Ray Tracer implements a hybrid method, the Rx is instead implemented as a point in space with an intersection program that only reports intersections if a ray intersects the Rx point within a small error radius ε. The received complex electric field is evaluated according to the Rx polarization, gain, and normalized radiation pattern. Before termination of the ray, the electric field is updated with an attenuation from the free space path loss over the total path and the phase shift caused by the distance traveled from the last intersection point.

3.2 Simulation of Reconfigurable Intelligent Surfaces

The RISs considered in this thesis are implemented using arrays of sub-wavelength patch elements that receive and re-radiate the signal with a real-time adjustable reflection

coefficient, thus applying an amplification and phase shift to the reflected wave. As described in Section 2.2, the propagation analysis of an RIS can be reduced to the following steps:

i) Compute the emitted electric field from the Tx toward each RIS element.

ii) Determine the impinging field at each RIS element based on the free space path loss factor and antenna characteristics of the RIS element.

iii) Compute the reemitted field from each RIS element toward the Rx.

iv) For each reemitted component, compute the electric field at the Rx based on the free space path loss factor, phase shift, and antenna characteristics of the Rx.

v) Apply the superposition principle to obtain the total electric field at the Rx.

The described process can be executed in the Ray Tracer by launching additional rays toward each RIS element that, when intersecting the RIS, relaunch toward the Rx from the points of intersection. To extend the Ray Tracer to support RISs, we first implemented a geometric and material representation of the RIS. Thereafter, we included a representation for RIS elements and extended the ray generation program. Finally, we derived a path loss model for the elements and created a material hit program that implemented the model and relaunched rays toward the Rx.

The geometric implementation of the RIS made use of the existing ZAG format described in Section 3.1.2. Additionally, a `RIS` material was created such that RISs can be defined as objects in a modeled environment.

To represent the RIS elements in the Ray Tracer, we defined additional inputs for the user to indicate the face of the RIS object on which the M elements are placed, and the relative position, dimensions, and reflection coefficients of the individual RIS elements. To account for the elements in the ray generation program, the element positions relative to the defined RIS object were mapped to the global coordinate system according to

$$\underline{\boldsymbol{u}}_m^{\text{global}} = \underline{\underline{\boldsymbol{A}}} \cdot \underline{\boldsymbol{u}}_m^{\text{relative}} + \underline{\boldsymbol{U}} \tag{3.6}$$

where $\underline{\boldsymbol{u}}_m^{\text{global}}$ is the position of the m-th element in the global coordinate system, $\underline{\boldsymbol{u}}_m^{\text{relative}}$ is the relative position of the m-th element in relation to the RIS center point and coordinate system depicted in Figure 3.5, and $\underline{\boldsymbol{U}}$ is the center point of the RIS face in the global coordinate system, i.e., the face on which the RIS elements are placed. $\underline{\underline{\boldsymbol{A}}}$ is the 3×3 orientation matrix of the RIS object, i.e., the global mapping of the local coordinate system defined in Figure 3.2. The mapped elements are stored in a data structure, containing their global positions, reflection coefficients, element dimensions, and surface normal. The element surface normal is the surface normal of the RIS object face on which the elements are placed. The ray generation program was thereafter extended to launch M rays toward the global position of every RIS element, i.e., in the direction $\frac{\underline{\boldsymbol{u}}_m^{\text{global}} - \underline{\boldsymbol{T}}}{||\underline{\boldsymbol{u}}_m^{\text{global}} - \underline{\boldsymbol{T}}||_2}$. To verify the correct mapping of elements, we implemented an additional feature that exports the locations of the mapped points for visualization in MATLAB.

Finally, a hit program for the RIS material was created to implement the path loss model described in Section 3.2.2 and relaunch the ray toward the Rx.

3.2.1 General Path Loss Model

To create a suitable path loss model for the AIT Ray Tracer, we started from the experimentally verified model from [28]:

$$P_\mathrm{r} = P_\mathrm{t}\frac{G_\mathrm{t}G_\mathrm{r}Gd_yd_z\lambda^2}{64\pi^3}\left|\sum_{m=1}^{M}\frac{\sqrt{F_m^\mathrm{c}}\Gamma_m}{d_m^\mathrm{t}d_m^\mathrm{r}}e^{\frac{-j2\pi(d_m^\mathrm{t}+d_m^\mathrm{r})}{\lambda}}\right|^2 \tag{3.7}$$

where d_y and d_z are the RIS element dimensions, G is the element gain, and Γ_m is the complex reflection coefficient of element m. The distance between the Tx and element m is d_m^t and the distance between element m and the Rx is d_m^r, as seen in Figure 3.5. The combined normalized radiation pattern F_m^c is defined as

$$F_m^\mathrm{c} = F_\mathrm{t}(\theta_m^\mathrm{t})F(\theta_m^\mathrm{e,t})F(\theta_m^\mathrm{e,r})F_\mathrm{r}(\theta_m^\mathrm{r}) \tag{3.8}$$

where $F_\mathrm{t}(.)$, $F_\mathrm{r}(.)$, and $F(.)$ are the normalized rotation symmetric antenna patterns for the Tx, Rx, and RIS elements, respectively. The model assumes that the polarization of the Tx and Rx are properly matched, even after reflection by the RIS. Additionally, it is assumed that there is LOS between Tx-RIS-Rx and that there are no additional MPCs than the direct reflection from the RIS elements.

In [10], the model was refined by providing an expression for the individual components of the combined radiation pattern

$$F_m^\mathrm{c} = (\cos\theta_m^\mathrm{t})^{\frac{G_\mathrm{t}}{2}-1}(\cos\theta_m^\mathrm{e,t})(\cos\theta_m^\mathrm{e,r})(\cos\theta_m^\mathrm{r})^{\frac{G_\mathrm{r}}{2}-1} \tag{3.9}$$

using (3.5) to model Tx and Rx as directional antennas and $\cos\theta$ to model the normalized power radiation pattern of RIS elements, where elevation θ is measured from the surface normal of the element. The cosine radiation pattern is illustrated in Figure 3.6. Additionally, an expression for the element gain

$$G = \frac{4\pi d_yd_z}{\lambda^2} \tag{3.10}$$

was provided, giving the general RIS path loss model

$$P_\mathrm{r} = P_\mathrm{t}\frac{G_\mathrm{t}G_\mathrm{r}(d_yd_z)^2}{16\pi^2}\left|\sum_{m=1}^{M}\frac{\sqrt{F_m^\mathrm{c}}\Gamma_m}{d_m^\mathrm{t}d_m^\mathrm{r}}e^{\frac{-j2\pi(d_m^\mathrm{t}+d_m^\mathrm{r})}{\lambda}}\right|^2. \tag{3.11}$$

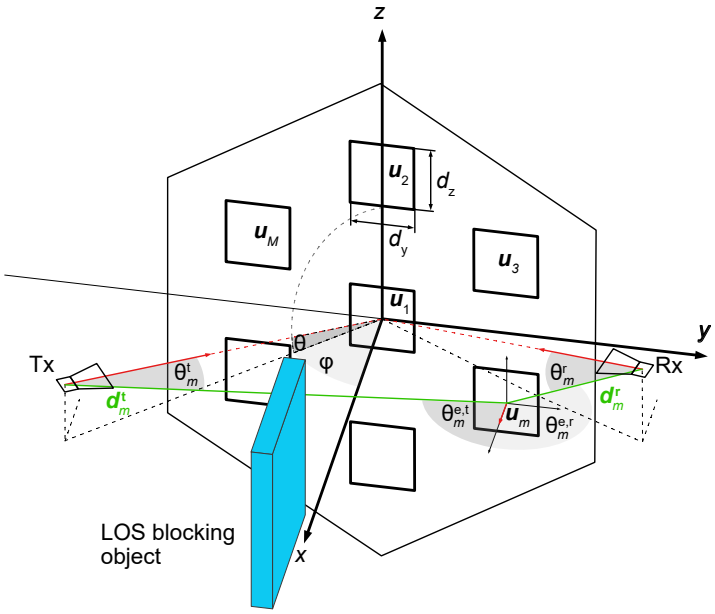

Figure 3.5: Illustration of an RIS with patch elements arranged in a hexagonal grid in the YZ-plane. Two horn antennas are directed toward the center of the RIS at the origin with blocked LOS. Angles $\theta_m^{e,\cdot}$ and $\theta_m^{\cdot}$ are measured from the surface normal of the elements and the orientation of the antennas, respectively.

3.2.2 Derivation of Refined Path Loss Model

Unlike the model described in Section 3.2.1, the AIT Ray Tracer works with electric fields. Additionally, the Ray Tracer is modular in the sense that the electric field is computed at each intersection with the environment, as seen in Figure 3.1. As a consequence, a closed-form expression is not compatible with the Ray Tracer. Therefore, we derived an alternative path loss model that computes the electric field for each ray at every step of its propagation path. Our proposed model builds on the ideas from [10] but has been compartmentalized for improved flexibility and better compatibility with the AIT Ray Tracer. As a result, our model can easily be applied to more complex scenarios, extended to incorporate other phenomena such as polarization, and combined with different propagation mechanisms.

By rewriting (2.8) we see that the initial electric field $\underline{\boldsymbol{E}}$ can be written in terms of the Poynting vector $\underline{\boldsymbol{S}}$

$$\underline{\boldsymbol{E}} = \sqrt{2\eta_0 \underline{\boldsymbol{S}}}\,. \tag{3.12}$$

Considering (2.1), we can express the magnitude of the electric field as

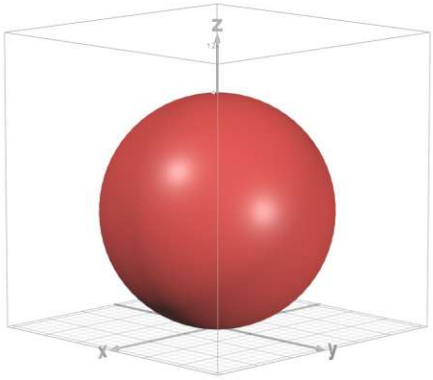

Figure 3.6: The normalized radiation pattern $F_{\text{RIS}} = \cos\theta$ of an RIS element.

$$E = \sqrt{\frac{2\eta_0 P_\text{t}}{4\pi d^2}} \tag{3.13}$$

at a distance d from the Tx. Accounting for the propagation phase alteration and the Tx antenna gain G_t and normalized radiation pattern $F_\text{t}(.)$, an expression for the emitted electric field

$$\underline{\boldsymbol{E}}_\text{t} = \left(\sqrt{\frac{2\eta_0 P_\text{t}}{4\pi d^2} G_\text{t} F_\text{t}(\theta_\text{t})} e^{\frac{-j2\pi d}{\lambda}}\right) \tag{3.14}$$

is obtained, where $\underline{\boldsymbol{E}}_\text{t}$ is a three-dimensional complex vector that considers the magnitude and polarization of the emitted electric field. Here, all formulas consider vertical polarization. The angle θ_t is the direction of the emitted field in relation to the Tx antenna orientation. To decouple the emitted field $\underline{\boldsymbol{E}}_t$ and the attenuation from the propagated distance, we define

$$E_0 = \sqrt{2\eta_0 P_\text{t}}\,. \tag{3.15}$$

We only consider the delay and attenuation of the signal once the ray hits an object or the Rx, such that the distance d is known. Therefore, rays launched toward the m-th RIS element center point have a field strength

$$\underline{\boldsymbol{E}}^\text{t}_m = \left(E_0 \sqrt{G_\text{t} F_\text{t}(\theta^\text{t}_m)}\right), \tag{3.16}$$

and the impinging electric field on element m is given by

$$\underline{\boldsymbol{E}}^{\text{RIS,in}}_m = \left(\sqrt{\frac{F(\theta^{\text{e,t}}_m) A_m}{4\pi (d^\text{t}_m)^2}} e^{\frac{-j2\pi d^\text{t}_m}{\lambda}}\right) \underline{\boldsymbol{E}}^\text{t}_m = \left(\sqrt{\frac{F(\theta^{\text{e,t}}_m) d_y d_z}{4\pi (d^\text{t}_m)^2}} e^{\frac{-j2\pi d^\text{t}_m}{\lambda}}\right) \underline{\boldsymbol{E}}^\text{t}_m\,. \tag{3.17}$$

In addition to the delay and attenuation of the signal at distance d, (3.17) accounts for the normalized radiation pattern $F(.)$ in the direction of the impinging wave, and effective area $A_m = d_y d_z$ of the RIS element. The reemitted electric field from the m-th element is given by

$$\underline{\boldsymbol{E}}_m^{\mathrm{RIS,out}} = \left(\sqrt{GF(\theta_m^{\mathrm{e,r}})}\Gamma_m \right) \underline{\boldsymbol{E}}_m^{\mathrm{RIS,in}} . \tag{3.18}$$

By combining (3.10) with (3.17), and (3.18), we obtain an expression for the RIS element's impact on the electric field:

$$\underline{\boldsymbol{E}}_m^{\mathrm{RIS}} = \left(\sqrt{F(\theta_m^{\mathrm{e,t}})F(\theta_m^{\mathrm{e,r}})} \frac{d_y d_z}{\lambda d_m^{\mathrm{t}}} \Gamma_m e^{\frac{-j2\pi d_m^{\mathrm{t}}}{\lambda}} \right) \underline{\boldsymbol{E}}_m^{\mathrm{t}} \tag{3.19}$$

The electric field at the Rx is computed according to (2.2) and (2.4):

$$E_m^{\mathrm{r}} = \left(\sqrt{\frac{A_{\mathrm{r}} G_{\mathrm{r}} F_{\mathrm{r}}(\theta_m^{\mathrm{r}})}{4\pi (d_m^{\mathrm{r}})^2}} e^{\frac{-j2\pi d_m^{\mathrm{r}}}{\lambda}} \right) \underline{\boldsymbol{E}}_m^{\mathrm{RIS}} = \left(\sqrt{G_{\mathrm{r}} F_{\mathrm{r}}(\theta_m^{\mathrm{r}})} \frac{\lambda}{4\pi d_m^{\mathrm{r}}} e^{\frac{-j2\pi d_m^{\mathrm{r}}}{\lambda}} \right) \underline{\boldsymbol{E}}_m^{\mathrm{RIS}} \tag{3.20}$$

The superposition of the received components from each element gives the total electric field at the Rx

$$E_{\mathrm{r}} = \sum_{m=1}^{M} E_m^{\mathrm{r}} \tag{3.21}$$

and the received power

$$P_{\mathrm{r}} = \frac{|E_{\mathrm{r}}|^2}{2\eta_0} . \tag{3.22}$$

Equations (3.16), (3.19), and (3.20) provide a complete description of the scenario in Figure 3.5, with (3.16) and (3.20) being equivalent to the Ray Tracer's antenna implementations discussed in Section 3.1.4. If the antenna and RIS polarizations are perfectly aligned, we obtain the original model from [10] by combining Equations (3.15), (3.16) and (3.19) to (3.22), given that no other MPCs are contributing to the received signal.

3.2.3 Supporting Reflections

Our flexible and compartmentalized model isolates the behavior of the RIS and is therefore easy to incorporate into existing Ray Tracers and extend to more complex scenarios. This was demonstrated by implementing additional functionality to consider the RIS together with reflective materials. RIS control algorithms often aim to improve the received signal strength by delaying components such that constructive interference is maximized at the location of the Rx. However, there typically exist several locations

where the signal components constructively interfere, resulting in a significant signal strength at multiple points in the environment. In an anechoic chamber or scene without IOs, such strong signal components from the RIS don't affect the received signal. In a reflective environment, however, the additional strong signal components may reflect toward the Rx and have a significant impact on the received signal power and channel impulse response (CIR).

As each RIS element acts as a transmitter, we can employ the image method as described in Section 2.3.2 and Section 3.1.3 to identify reflection points between the RIS and Rx. Similarly, we can use the image method to identify reflected components from the Tx impinging on the RIS. However, in this thesis, we focus on directional Tx antennas focusing toward the RIS, therefore, such components are of less interest.

To efficiently identify valid reflection paths between the RIS and Rx, we don't execute the entire procedure described in Section 3.1.3 for every RIS element. Instead, we search for valid permutations of surfaces forming unblocked paths only between the RIS face center point $\underline{\boldsymbol{U}}$ and the Rx position $\underline{\boldsymbol{R}}$, as seen in Figure 3.7a. Thereafter, we perform the image method on each RIS element only for the valid and unblocked surface permutations, as in Figure 3.7b.

Initially, rays were only relaunched from the RIS toward the Rx. To support reflections from the RIS, we, therefore, defined a new variable, `target`, specifying the location of the point toward which the ray should be relaunched, i.e., either the Rx or a computed reflection point. Thereafter, rays are specularly reflected until the Rx is hit or the maximum number of reflections is met.

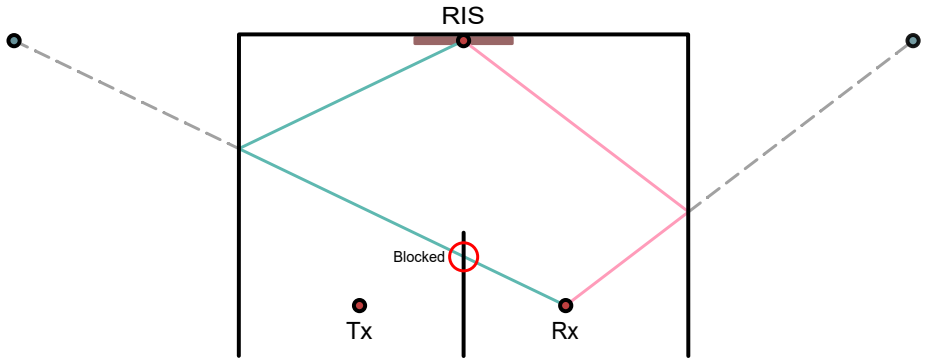

(a) Identifying surface permutations for unblocked paths between the RIS center point and the Rx using the image method. The blue path is blocked, and will therefore not be considered in the next step.

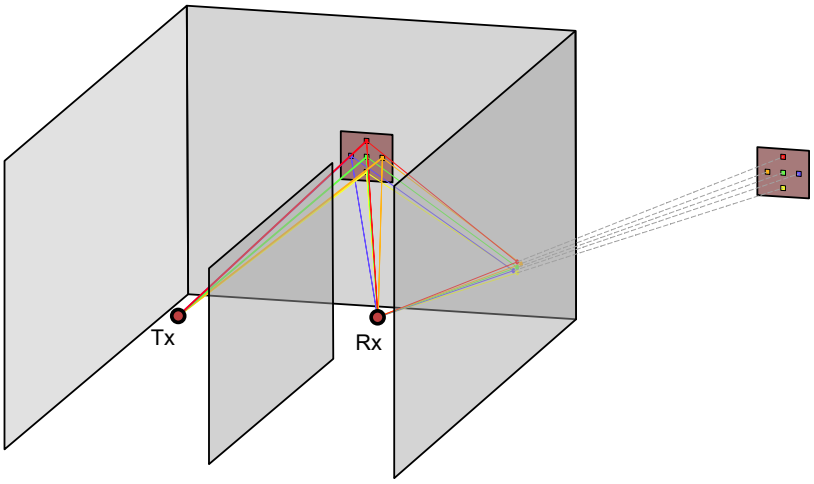

(b) Performing the image method on every RIS element only for unblocked surface permutations.

Figure 3.7: Procedure for identifying valid reflection paths between the RIS and Rx in two steps: first identify unblocked paths (a), then perform the image method only for unblocked paths (b).

Chapter 4

Simulations

To verify the implementation of reconfigurable intelligent surfaces in the AIT Ray Tracer described in the previous Chapter, we simulated and evaluated the two scenarios. The first considers an RIS in an isolated environment, and the second accounts for reflections between the RIS and the receiver on metallic walls. This Chapter presents the simulation setup and model parameters used for verification.

4.1 Anechoic Chamber

We performed a simulation of the RIS in an isolated environment and compared it to the experimentally verified path loss model from [10] and measurements from [11]. The isolated environment consists of MPCs between the antennas exclusively through the RIS. The direct path between the Tx and Rx is thus blocked, and there exist no objects in the environment with which the electric field may interact. Additionally, LOS can be assumed between the two antennas and every RIS element. To align with the assumptions made by [10], polarization is configured to be perfectly matched between the two antennas.

The measurement setup equivalent to the described scenario is shown in Figure 4.1 from [11]. The two antennas and an RIS were installed in an anechoic chamber with a panel mounted to block the direct path from the Tx and Rx. The walls and the blocking panel were covered with microwave absorbers to minimize undesired reflected electromagnetic waves. Furthermore, vertically polarized directional horn antennas were positioned facing the RIS to maximize the emitted and received signals. To measure the beam pattern in a sphere around the RIS, the Tx could be moved in azimuth and the RIS could rotate in all three axes. The outgoing signal from the RIS may be horizontally or vertically polarized, depending on the mode in which the RIS operates. The antennas could therefore be rotated by 90° to analyze polarization in both modes.

To empirically obtain the beam pattern of the RIS for a set element configuration, [11] computed the received signal power from the measured channel impulse response for every azimuth ϕ and elevation θ in a range $-45° \leq \phi \leq 45°$ and $-45° \leq \theta \leq 45°$. In numerical simulation, the beam pattern of the RIS was obtained by evaluating the received signal power at every position of the Rx in the range, sampled in steps of 1°, while the Tx and RIS were kept at fixed positions, as illustrated in Figure 4.2. The RIS was configured to maximize the reflection toward $\underline{\boldsymbol{R}}_{\text{opt}} = (1.7\,\text{m}, 15°, 30°)$ in relation to a RIS centered at $\underline{\boldsymbol{U}} = (0, 0, 0)$, with an impinging wave from the Tx at $\underline{\boldsymbol{T}} = (1.7\,\text{m}, -25°, 0°)$.

Beam patterns obtained when simulating the described scenario in the AIT Ray Tracer were expected to be comparable to those obtained in [11]. Furthermore, they were

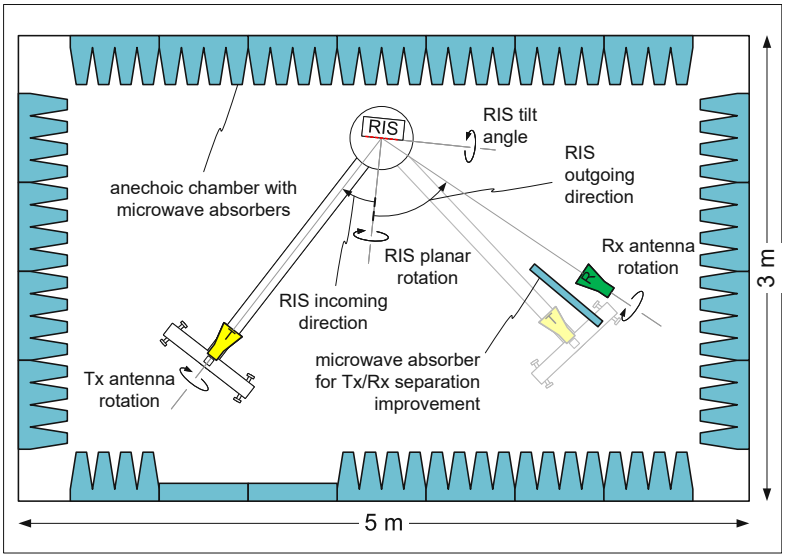

Figure 4.1: The measurement setup in an anechoic chamber from [11] to determine the beam pattern of an active RIS. The Tx can be moved in azimuth, and the Rx and RIS are mounted at a fixed location. The Tx and Rx can be rotated by 90° to analyze horizontal and vertical polarization, and the RIS can be rotated about every axes.

expected to be in accordance with the RIS path loss model from [10]. In the subsequent sections, we describe the simulation setup in the Ray Tracer.

4.1.1 Environment

The measurement environment in Figure 4.1 was imported to the Ray Tracer by providing the geometries in ZAG format with their corresponding material parameters as described in Section 3.1.2. Walls mounted with absorbers are not expected to reflect impinging electromagnetic waves and are therefore equivalent to the absence of IOs. For optimal efficiency, walls covered with absorbers were thus omitted from the ZAG input, significantly reducing the number of required intersection checks and the general complexity of the scenario. As ray types are included in the results, LOS rays may be removed in post-processing. Therefore, the blocking panel could be omitted from the geometry, simplifying the simulation and resolving issues that arise when the panel overlaps the Rx antenna for specific sampling points.

Thus, the only geometry object required to simulate the anechoic chamber was the RIS, implemented as a $10.8 \times 10.8 \times 1\,\text{cm}$ block in ZAG format of `RIS` material. The front face of the block was centered at $\underline{\boldsymbol{U}} = (0, 0, 0)$ with surface normal $\underline{\boldsymbol{n}} = (1, 0, 0)$. Typically, materials implemented in the Ray Tracer require several material parameters such as permittivity, conductivity, diffuse scatter coefficients, and various model parameters. These must be defined to correctly evaluate the material's impact on the electric field

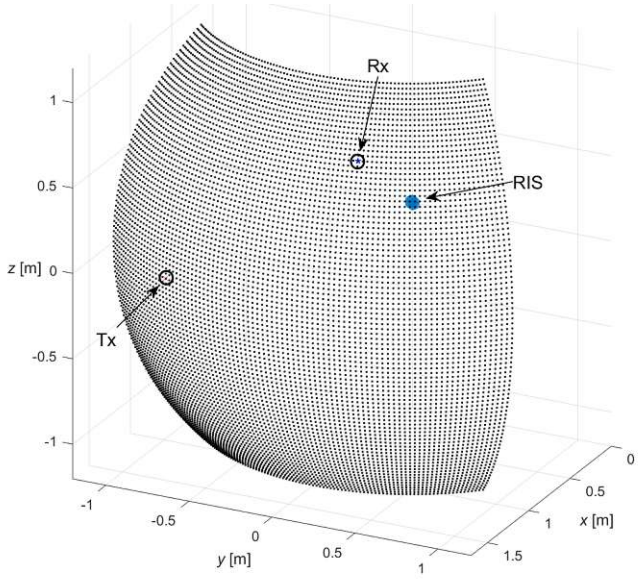

Figure 4.2: Numerical simulation setup for determining the beam pattern of an RIS by measuring the received signal power at sample points from a sphere of radius $r = 1.7\,\mathrm{m}$ around the RIS in a range $-45° \leq \phi \leq 45°$ and $-45° \leq \theta \leq 45°$. The Tx was placed at $\underline{\boldsymbol{T}} = (1.7\,\mathrm{m}, -25°, 0°)$ and the Rx at $\underline{\boldsymbol{R}}_{\mathrm{opt}} = (1.7\,\mathrm{m}, 15°, 30°)$ from the RIS.

upon reflection, diffraction, or diffuse scattering. As such mechanisms aren't considered for RIS objects, the material specification was only used to identify the existence of an object of `RIS` material, ignoring any additional material parameters. The complete input geometry and intended antenna setup can be seen in Figure 4.3.

4.1.2 Configurations

A configuration file was passed to the Ray Tracer providing antenna and RIS specifications, ray tracing parameters, and other relevant data. We developed a MATLAB script to automate the generation of configuration files, where the user specifies the antenna gains, the sampling range, sampling step size, and the positions of the Tx and RIS. The script computes antenna model coefficients, positions, and orientations for each sampling point in the range. An overview of the configuration parameters can be seen in Table 4.1.

Antenna Models

The directional horn antennas used for measurement in [11] were implemented in the Ray Tracer using the directional antenna model in (3.5), with directional antenna gain G and cosine exponent $k = \frac{G}{2} - 1$. The antennas have a directional gain $G_{\mathrm{t}} = G_{\mathrm{r}} = 19\,\mathrm{dB}$, and the transmit power P_{t} is $10\,\mathrm{dBm}$. The antennas are oriented such that their main lobe at

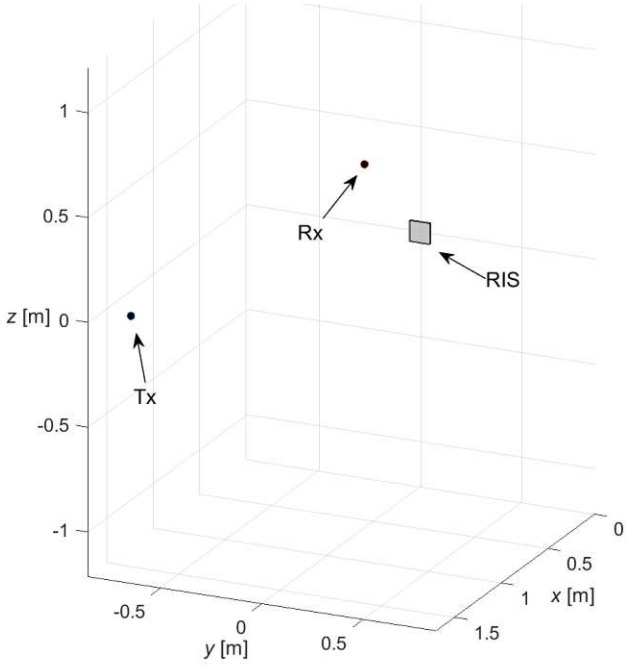

Figure 4.3: Anechoic chamber modeled in ZAG format for the AIT Ray Tracer. The geometry consists of an RIS block with the front face centered at the origin. Tx and Rx antennas are positioned at $\underline{\boldsymbol{T}} = (1.54, -0.72, 0)$ and $\underline{\boldsymbol{R}} = (1.42, 0.38, 0.85)$, respectively.

$\theta = 0°$, measured from the z-axis of the antenna orientation matrix, is directed toward the center of the RIS. Focusing the horn antennas toward the RIS center point $\underline{\boldsymbol{U}}$ is thus equivalent to aligning the antennas' local z-axes with the direction vectors $\underline{\boldsymbol{r}}_{\mathrm{t}} = \frac{\underline{\boldsymbol{U}} - \underline{\boldsymbol{T}}}{||\underline{\boldsymbol{U}} - \underline{\boldsymbol{T}}||_2}$ and $\underline{\boldsymbol{r}}_{\mathrm{r}} = \frac{\underline{\boldsymbol{U}} - \underline{\boldsymbol{R}}}{||\underline{\boldsymbol{U}} - \underline{\boldsymbol{R}}||_2}$ for the Tx and Rx, respectively. This is done by performing extrinsic rotations on the antenna orientation matrix, i.e., rotations in the global coordinate system, about the y- and z-axes according to

$$\underline{\underline{\boldsymbol{R}}}(\theta, \phi) = \underline{\underline{\boldsymbol{R}}}_z(\phi)\underline{\underline{\boldsymbol{R}}}_y(\theta) \tag{4.1}$$

where

$$\underline{\underline{\boldsymbol{R}}}_y(\theta) = \begin{pmatrix} \cos\theta & 0 & \sin\theta \\ 0 & 1 & 0 \\ -\sin\theta & 0 & \cos\theta \end{pmatrix}, \quad \underline{\underline{\boldsymbol{R}}}_z(\phi) = \begin{pmatrix} \cos\phi & -\sin\phi & 0 \\ \sin\phi & \cos\phi & 0 \\ 0 & 0 & 1 \end{pmatrix} \tag{4.2}$$

are the basic 3D rotation matrices about the y- and z-axes, respectively. The angle ϕ is the azimuth of $\underline{\boldsymbol{r}}$ with respect to the global coordinate system, and θ is the elevation.

The Rx position and antenna orientation matrix were computed for every sample in the ranges $-45° \leq \phi \leq 45°$ and $-45° \leq \theta \leq 45°$ with a step size of 1°. The Tx position and antenna orientation matrix were computed once for $\underline{\boldsymbol{T}} = (1.7\,\mathrm{m} - 25°, 0°)$.

Technical Details of the RIS

The active RIS used in [11], seen in Figure 2.5, consists of $M = 37$ patch antenna elements with an effective element size $d_y = d_z = 6.6\,\text{mm}$, arranged in a hexagonal grid. The RIS has two operating modes: a reflective mode where the reflection coefficients apply an attenuation and phase shift to the impinging wave, and an active mode in which the elements are either switched on or off, providing an amplification to the signal if switched on. In both modes, each element can have one of two states. In reflective mode

$$\Gamma_m^{\text{r}} \in \{(-4\,\text{dB}, \angle 0°), (-4\,\text{dB}, \angle 67°)\} \tag{4.3}$$

and in active mode

$$\Gamma_m^{\text{a}} \in \{(+3\,\text{dB}, \angle 0°), (+0\,\text{dB}, \angle 0°)\}\,. \tag{4.4}$$

The RIS element configurations for the two modes were computed according to the control algorithm defined in [11]. For a desired main lobe focusing on the Rx in the described scenario, the elements were configured as depicted in Figure 4.4. The element locations and their corresponding complex reflection coefficients were passed to the Ray Tracer in additional input files.

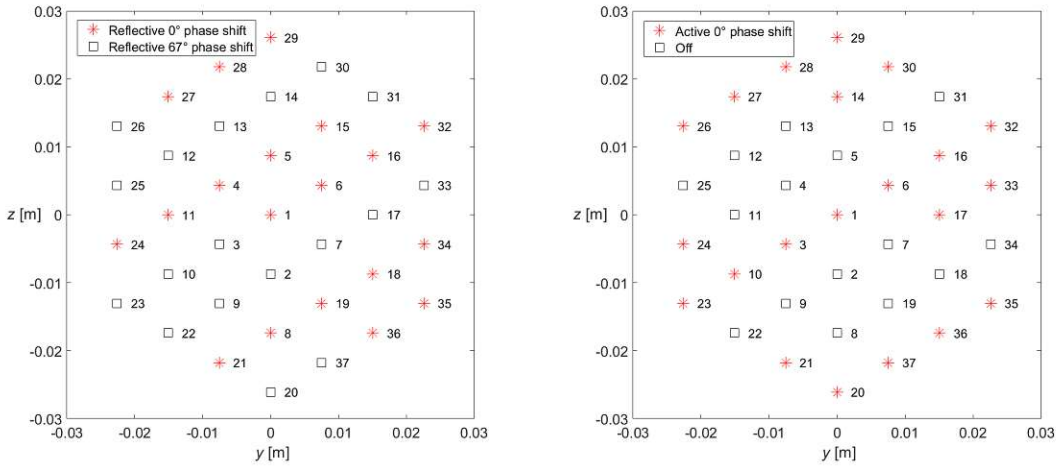

(a) Reflective mode (b) Active mode

Figure 4.4: The configurations of the RIS with $M = 37$ elements in reflective (left) and active (right) modes for a desired main lobe focusing on $\underline{\boldsymbol{R}}_{\text{opt}} = (1.7\,\text{m}, 15°, 30°)$ with an impinging wave from the Tx at $\underline{\boldsymbol{T}} = (1.7\,\text{m}, -25°, 0°)$ from the RIS.

4.2 Reflective Environment

For realistic use cases, the environments in which RISs are employed are not isolated from reflections and other propagation mechanisms. Although the attenuation from free space

Table 4.1: Configuration parameters and simulation setup for RIS in an anechoic chamber.

Parameter	**Definition**
$f = 25.8\,\mathrm{GHz}$	center frequency
$n_{\max} = 1$	maximum reflection order from Tx
$F_{\mathrm{t}}(\theta) = F_{\cos}(\theta)$	Tx normalized field pattern
$F_{\mathrm{r}}(\theta) = F_{\cos}(\theta)$	Rx normalized field pattern
$P_{\mathrm{t}} = 10\,\mathrm{dBm}$	Tx transmit power
$G_{\mathrm{t}}, G_{\mathrm{r}} = 19\,\mathrm{dB}$	Tx and Rx antenna gain
$\underline{\boldsymbol{T}} = (1.7\,\mathrm{m}, -25°, 0°)$	Tx position in relation to RIS
$\underline{\boldsymbol{R}}_{\mathrm{opt}} = (1.7\,\mathrm{m}, 15°, 30°)$	intended Rx position in relation to RIS
$-45° \leq \phi \leq 45°$	azimuth sampling range
$-45° \leq \theta \leq 45°$	elevation sampling range
$n_{\mathrm{step}} = 1°$	sampling step size
$M = 37$	number of RIS elements
$n_{\max}^{\mathrm{RIS}} = 0$	maximum reflection order from RIS
$d_y,\, d_z = 6.6\,\mathrm{mm}$	effective RIS element size
$\Gamma_m^{\mathrm{r}} \in \{(-4\,\mathrm{dB}, \angle 0°), (-4\,\mathrm{dB}, \angle 67°)\}$	reflection coefficients in reflective mode
$\Gamma_m^{\mathrm{a}} \in \{(+3\,\mathrm{dB}, \angle 0°), (+0\,\mathrm{dB}, \angle 0°)\}$	reflection coefficients in active mode

path loss and interaction with objects is high for mmWaves, the impact of interference from MPCs in an environment can significantly affect the received signal power and CIR. Signal components from an active RIS on reflective objects may have a particularly large contribution to the behavior of the channel due to the amplification of components. Therefore, it was of interest to investigate simulations where such components were taken into account.

For this scenario, we simulated a reflective environment in which metallic walls were mounted on the sides and opposite of the RIS. In practice, receivers are often mobile and must receive signals from any incoming direction, therefore, we chose an isotropic Rx antenna moving in an XY-plane below the RIS, as seen in Figure 4.5. As in the anechoic chamber, a fixed directional Tx horn antenna was positioned to maximize the emitted signal in the direction of the RIS, assuming that the direct path between the Tx and Rx may be blocked.

To evaluate the impact of reflected components from the RIS, we executed and compared two simulations: the first in which only MPCs with a direct path between the RIS and Rx were considered, and the second which considered every MPC from the RIS up to a maximum order of reflection. The RIS was configured to maximize the signal toward $\underline{\boldsymbol{R}}_{\mathrm{opt}} = (1.4\,\mathrm{m}, 10°, -14.68°)$, reflected from a Tx at $\underline{\boldsymbol{d}}_{\mathrm{t}} = (1.68\,\mathrm{m}, -28°, 0°)$ from the RIS.

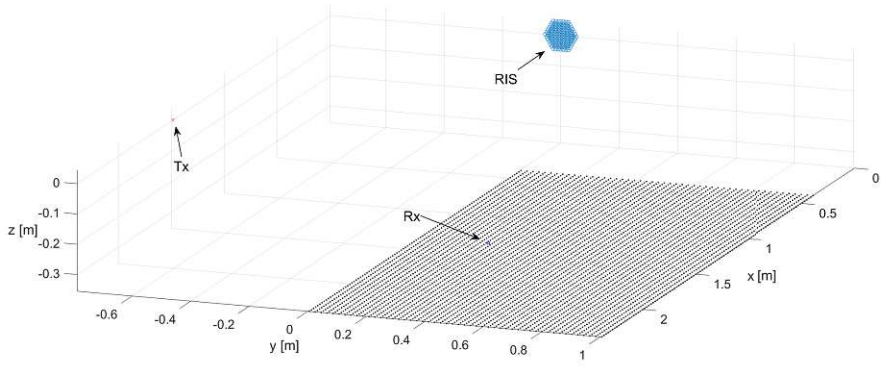

Figure 4.5: Numerical simulation setup for determining the received signal power from an RIS by measuring the received signal power at sample points from the XY-plane in a range $0 \leq x \leq 2\,\mathrm{m}$ and $0 \leq y \leq 1\,\mathrm{m}$ at $z = -0.355\,\mathrm{m}$ from the RIS, with an offset $\underline{\boldsymbol{P}} = (-2.39, -1.005, -0.355)\,\mathrm{m}$ from the RIS.

4.2.1 Environment

To model the described environment in the Ray Tracer, three metallic walls and an RIS object were defined in ZAG format, as shown in Figure 4.6. The blocks of `metal` material constructed a $2.5 \times 2.3 \times 1\,\mathrm{m}$ room with an opening in which a $20 \times 20 \times 2\,\mathrm{cm}$ block of `RIS` material was defined. The front face of the RIS block was centered at $\underline{\boldsymbol{U}} = (2.58, 1.4, 0.5)$ with surface normal $\underline{\boldsymbol{n}} = (-1, 0, 0)$. The `metal` material was defined as a perfect electrical conductor (PEC) with relative permittivity $\varepsilon_r = 1.0$ and conductivity $\sigma = 10^7 \frac{\mathrm{S}}{\mathrm{m}}$. As in the simulation of the anechoic chamber, no blocking panel was included to reduce the complexity of the scenario as undesired components can be excluded from the total electric field in post-processing.

4.2.2 Configurations

To automate the generation of configuration files for the simulation, we developed a MATLAB script. The user specifies the antenna gains, the positions of the Tx and RIS, and the maximum order of reflection for RIS components. Additionally, the sampling range, step size, and XY-plane offset must be defined. The script computes the antenna model coefficients, the Tx position and orientation, and the position of the Rx for every sample point in the range. An overview of the configuration parameters can be seen in Table 4.2.

Antenna Models

The transmitter is implemented with the directional antenna model in (3.5), with cosine exponent $k = \frac{G_\mathrm{t}}{2} - 1$, directional antenna gain $G_\mathrm{t} = 19\,\mathrm{dB}$, and transmit power $P_\mathrm{t} = 10\,\mathrm{dBm}$. The antenna orientation is set such that the main lobe at $\theta = 0$ is focused on

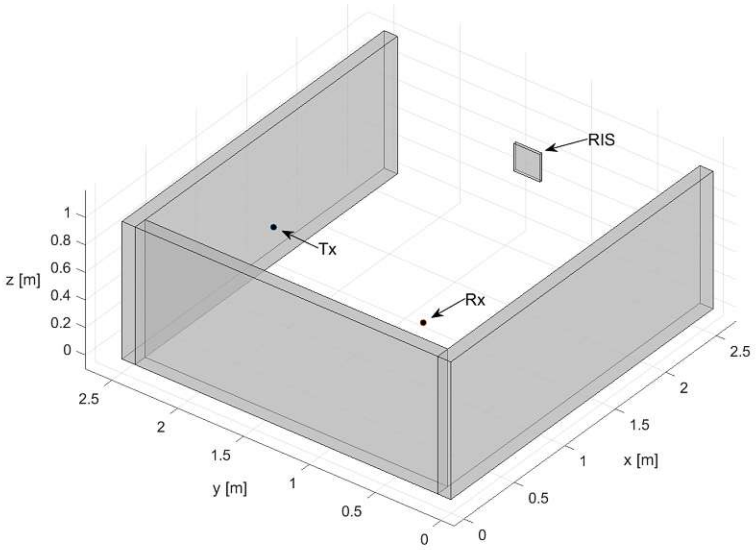

Figure 4.6: Reflective environment modeled in ZAG format for the AIT Ray Tracer. The geometry consists of an RIS block with the front face centered at $\underline{\boldsymbol{U}} = (2.58, 1.4, 0.5)$, and three metallic blocks constructing walls in a room of dimensions $2.5 \times 2.3 \times 1\,\mathrm{m}$. Tx and Rx antennas are positioned at $\underline{\boldsymbol{T}} = (1.10, 2.19, 0.5)$ and $\underline{\boldsymbol{R}} = (1.25, 1.16, 0.145)$, respectively.

the RIS center point $\underline{\boldsymbol{U}}$ using (4.1), as described in Section 4.1.2. The Rx antenna is implemented with the isotropic antenna model in (3.3) with antenna gain $G_\mathrm{r} = 5.2\,\mathrm{dB}$.

The orientation and position of the Tx are computed once for $\underline{\boldsymbol{T}} = (1.68\,\mathrm{m}, -28°, 0°)$ in relation to the RIS. The position of the Rx is computed for every sample in the ranges $0 \leq x \leq 2\,\mathrm{m}$ and $0 \leq y \leq 1\,\mathrm{m}$ with a sampling distance of $2\,\mathrm{cm}$ and an offset $\underline{\boldsymbol{P}} = (-2.39, -1.005, -0.355)\,\mathrm{m}$ from $\underline{\boldsymbol{U}}$.

Technical Details of the RIS

The active RIS used in the reflective environment consists of $M = 127$ patch antenna elements with an effective element size $d_y = d_z = 6.6\,\mathrm{mm}$, arranged in a hexagonal grid. As the RIS operates in active mode, each element is either switched on or off, providing an amplification of $3\,\mathrm{dB}$ if switched on. The reflection coefficient is thus

$$\Gamma_m \in \{(+3\,\mathrm{dB}, \angle 0°), (+0\,\mathrm{dB}, \angle 0°)\}\,. \tag{4.5}$$

As for the simulation of the RIS in an isolated environment, the element configuration is computed as in [11]. For a main lobe focusing on $\underline{\boldsymbol{R}}_\mathrm{opt} = (1.4\,\mathrm{m}, 10°, -14.68°)$, the elements are configured according to Figure 4.7.

Table 4.2: Configuration parameters and simulation setup for RIS in a reflective environment.

Parameter	**Definition**
$f = 25.8\,\mathrm{GHz}$	center frequency
$n_{\max} = 2$	maximum reflection order from Tx
$F_{\mathrm{t}}(\theta) = F_{\cos}(\theta)$	Tx normalized field pattern
$F_{\mathrm{r}}(\theta) = F_{\mathrm{isotropic}}(\theta)$	Rx normalized field pattern
$P_{\mathrm{t}} = 10\,\mathrm{dBm}$	Tx transmit power
$G_{\mathrm{t}} = 19\,\mathrm{dB}$	Tx antenna gain
$G_{\mathrm{t}} = 5.2\,\mathrm{dB}$	Rx antenna gain
$\underline{\boldsymbol{T}} = (1.68\,\mathrm{m}, -28°, 0°)$	Tx position in relation to RIS
$\underline{\boldsymbol{R}}_{\mathrm{opt}} = (1.4\,\mathrm{m}, 10°, -14.68°)$	intended Rx position in relation to RIS
$0 \leq x \leq 2\,\mathrm{m}$	x sampling range
$0 \leq y \leq 1\,\mathrm{m}$	y sampling range
$n_{\mathrm{step}} = 2\,\mathrm{cm}$	sampling step size
$\underline{\boldsymbol{P}} = (-2.39, -1.005, -0.355)\,\mathrm{m}$	sampling offset from RIS
$M = 127$	number of RIS elements
$n^{\mathrm{RIS}}_{1,\max} = 0$	maximum reflection order from RIS in case 1
$n^{\mathrm{RIS}}_{2,\max} = 2$	maximum reflection order from RIS in case 2
$d_y,\, d_z = 6.6\,\mathrm{mm}$	effective RIS element size
$\Gamma_m \in \{(+3\,\mathrm{dB}, \angle 0°), (+0\,\mathrm{dB}, \angle 0°)\}$	reflection coefficients
$\varepsilon_{r,\mathrm{metal}} = 1.0$	relative permittivity of `metal` material
$\sigma_{\mathrm{metal}} = 10^7\,\frac{\mathrm{S}}{\mathrm{m}}$	conductivity of `metal` material

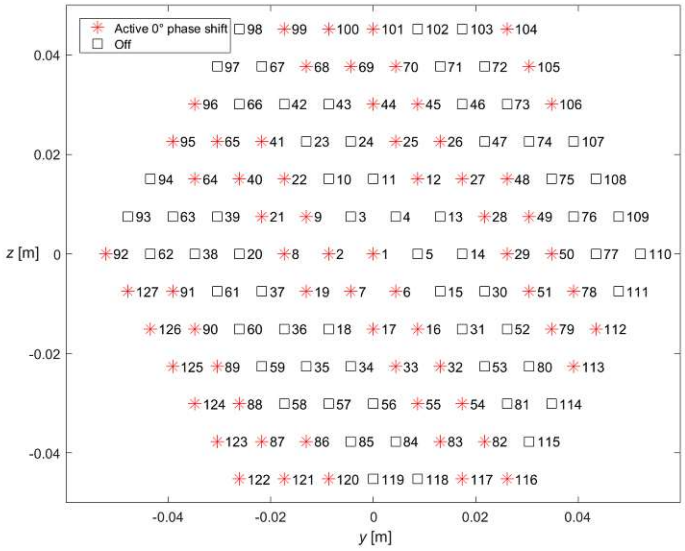

Figure 4.7: The configurations of an RIS with $M = 127$ elements for a desired main lobe focusing on $\underline{\boldsymbol{R}}_{\text{opt}} = (1.4\,\text{m}, 10°, -14.68°)$ and an impinging wave from the Tx at $\underline{\boldsymbol{T}} = (1.68\,\text{m}, -28°, 0°)$ from the RIS.

Chapter 5

Results

In this Chapter, we present the results obtained from the simulation of an RIS in an anechoic chamber and a reflective environment, using the AIT Ray Tracer. The results are evaluated using our path visualization tool and by comparison with measurements and a simpler numerical simulation software.

5.1 Validation of Results

For every simulated scenario, the AIT Ray Tracer outputs a file with the complex electric field, delay, direction of arrival, frequency, and ray type of each MPC. Furthermore, we implemented options to export global RIS element locations and intersection data for path visualization in MATLAB. The three files provide various tools to analyze the given environment and simulation setup, further described in this Section.

5.1.1 Path Visualization

The path visualization tool provides users with helpful insights when configuring simulations and assists developers in verifying correctness when implementing new features. For the export of data for path visualization, the macro `EXPORT_VISUALIZATION_DATA` must be defined in the preprocessor during compilation. Upon execution, every hit program writes intersection data to a buffer that is copied back to the CPU at the end of ray tracing. The data includes the ray type and intersection points at every reflection for each ray, required to assemble every path in post-processing. For optimal performance, this feature should be disabled as additional device-host memory transfer affects the runtime of the software. As an extension of the path visualization tool, the global RIS element locations can be exported by defining the macro `EXPORT_GLOBAL_RISPOINTS` to verify the correct mapping of elements.

For validation of our implementation, the RIS point and path visualization tool was used to verify the correctness of ray launching. The expected behavior is that for each identified reflection from the RIS to the Rx, including LOS, one ray per element is launched toward the corresponding element, and relaunched toward the corresponding target point. The intersection points of launched rays on the RIS should thus be consistent with the exported RIS element points, and the intersection points of relaunched rays should correlate to points that were computed with the image method.

5.1.2 Processing Electric Field Components

The general output of the Ray Tracer is a file with the complex electric field, delay, direction of arrival, frequency, and ray type of each MPC and stationary time step, providing an extensive description of the channel.

Firstly, the total electric field at the receiver is given by the superposition of the individual components, i.e.,

$$E_k = \sum_{i=1}^{N_k} E_{k,i} \tag{5.1}$$

where N_k is the total number of MPCs at time instant k, and $E_{k,i}$ is the complex electric field of the i-th MPC from the Tx to the Rx, already accounting for the effective area of the Rx antenna. Additionally, the received signal power can be computed according to

$$P_k = \frac{|E_k|^2}{2\eta_0} \tag{5.2}$$

in Watts, and

$$P_k^{\mathrm{dBm}} = 10 \log_{10} \left(\frac{P_k}{1\mathrm{mW}} \right) \tag{5.3}$$

in dBm. As the complex electric field, delay, and carrier frequency are exported for each MPC and time instance, it is possible to compute the discrete time- and frequency variant channel transfer function (CTF). The CTF provides sufficient information about the channel to obtain a wide range of channel descriptions and parameters as described in [9] and [13], e.g., the channel impulse response (CIR), power delay profile (PDP), and Doppler spectral density (DSD).

For evaluation of the RIS path loss model presented in Section 3.2.2, we collect the received signal power at different positions in a predefined range, as described in Chapter 4. The received signal components were thus processed according to (5.1) and (5.2) for $k = 1$ at each sampled position, and stored in a 2D array for plotting. Undesired components, e.g., the LOS, were omitted from (5.1).

5.1.3 Comparing Results

To assess the accuracy of our implementation we evaluated the error and correlation of our results with (3.11), i.e., the verified model from [10], and measurements from [11].

We computed the mean square error (MSE)

$$\mathrm{MSE} = \frac{1}{n} \sum_{i=1}^{n} \left(P_i^{\mathrm{ref}} - P_i^{\mathrm{RT}} \right)^2 \tag{5.4}$$

where n is the number of sampling points, P_i^{ref} is the received power at point i in the reference model or measurement, and P_i^{RT} is the received power at point i obtained by the Ray Tracer. Large outliers significantly affect the score as error terms are squared,

therefore, the MSE provides insights to detect inconsistencies in our model or bugs in the implementation. For facilitated interpretation of the results, we additionally computed the mean absolute percentage error (MAPE)

$$\text{MAPE} = \frac{1}{n}\sum_{i=1}^{n}\left|\frac{P_i^{\text{ref}} - P_i^{\text{RT}}}{P_i^{\text{ref}}}\right| \tag{5.5}$$

as it expresses the error in relative terms.

5.2 Anechoic Chamber

The simulation setup for determining the beam pattern of an RIS in an anechoic chamber is described in Section 4.1. Following, we present the results of the Ray Tracer through inspection of ray launching. Furthermore, we compare the obtained beam pattern to measurements from [11] and a simpler MATLAB beam pattern simulation software based on the path loss model from [10].

5.2.1 Verification of Ray Launching

To verify the implementation of ray launching and global mapping of RIS elements, we inspected the generated paths for the intended setup, i.e., with $\underline{\boldsymbol{T}} = (1.54, -0.72, 0)$ and $\underline{\boldsymbol{R}} = (1.42, 0.38, 0.85)$, using the path visualization MATLAB program. The generated plot can be seen in Figure 5.1a with a closeup of the RIS in Figure 5.1b. As the blocking panel was omitted from the geometry, there was one LOS ray directly between the Tx and Rx. Furthermore, the expected 37 RIS rays were launched toward their corresponding element. Thereafter, they intersected the RIS object on the front face at the element points marked in red and were relaunched toward the Rx. In addition, we confirmed that for every sample point in the defined range, exactly 38 rays, one of LOS type and 37 of RIS type, were generated by the Tx and received by the Rx. No rays of reflection type were launched toward the RIS for any position of the Rx, as the maximum reflection order from the Tx was set to zero. As the implementation ensures that only components considered in our derived path loss model are relaunched from the RIS, any identified reflection, diffraction, or scatter points on the RIS would be terminated upon intersection.

5.2.2 Empirical Evaluation

The beam patterns of the active RIS in reflective and active modes were obtained by computing and plotting the received signal power for every sampling point by applying Equations (5.1) to (5.3) for every MPC of RIS type. In this section, we present the obtained beam patterns and compare them to those obtained in measurements from [11].

Reflective Mode

The beam pattern of the active RIS operating in reflective mode is plotted in Figure 5.2. Figure 5.2a shows the beam pattern obtained from numerical simulation using the AIT

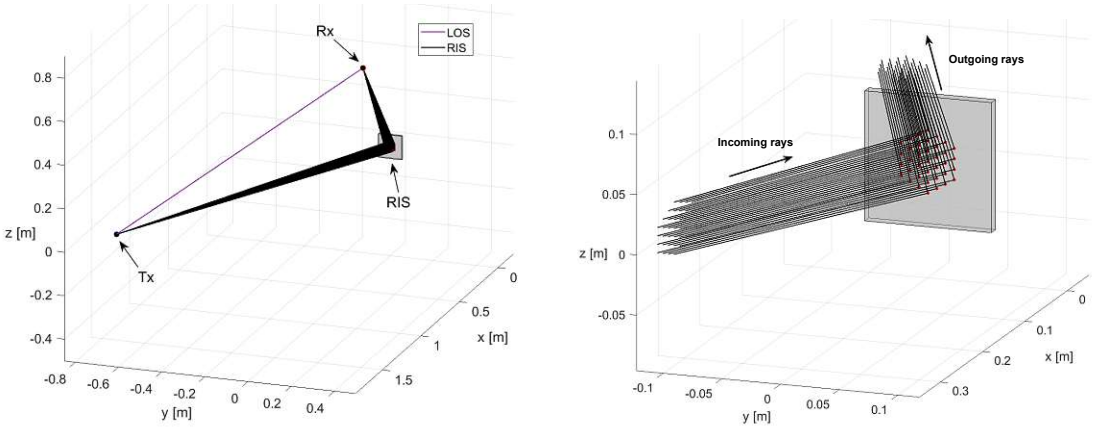

(a) Full environment

(b) Closeup on RIS

Figure 5.1: Path visualization for an RIS with 37 elements in an isolated environment with $\underline{\boldsymbol{T}} = (1.54, -0.72, 0)$ and $\underline{\boldsymbol{R}} = (1.42, 0.38, 0.85)$. The LOS ray is plotted in purple, RIS rays in black, and globally mapped RIS element points in red.

Ray Tracer, and Figure 5.2b shows the measured beam pattern from [11]. The specular reflection is distinct in the simulated and measured beam patterns, with a received power of approximately $-50\,\text{dBm}$. The RIS furthermore reflects the outgoing signal toward the desired direction $(\phi, \theta) = (15°, 30°)$ with an approximate gain of $-55\,\text{dBm}$ in both simulation and measurement. Additionally, the Ray Tracer implementation successfully identifies a weaker side lobe at $(42°, -29°)$ of approximately $-60\,\text{dBm}$. As described in [11], the specular reflection is caused by the limited phase shift of 67°, and the weaker side lobe is caused by the finite size of the RIS and the element spacing. The most important components of our simulated beam pattern correspond very well to the measurement. Several weaker side lobes of $-70\,\text{dBm}$ can also be identified in both plots, despite being more difficult to identify in measurement. Our implementation of the RIS in the AIT Ray Tracer could thus successfully generate the beam pattern of the RIS operating in reflective mode.

Active Mode

The simulated and measured beam patterns of the RIS operating in active mode are plotted in Figure 5.3. Figure 5.3a shows the beam pattern from simulation with the AIT Ray Tracer, and Figure 5.3b shows the measured beam pattern from [11]. Similar to the reflective case, the three particularly strong lobes can be identified in both measurement and simulation. Furthermore, several weaker side lobes with a received signal power around -53 to $-51\,\text{dBm}$ can be identified in both measurement and simulation. As the weaker side lobe at $(42°, -29°)$ is caused by factors independent of the operation mode, its appearance in the active mode is expected in both simulation and measurement. In active mode, the weaker side lobe has an approximate signal power of $-45\,\text{dBm}$. Likewise,

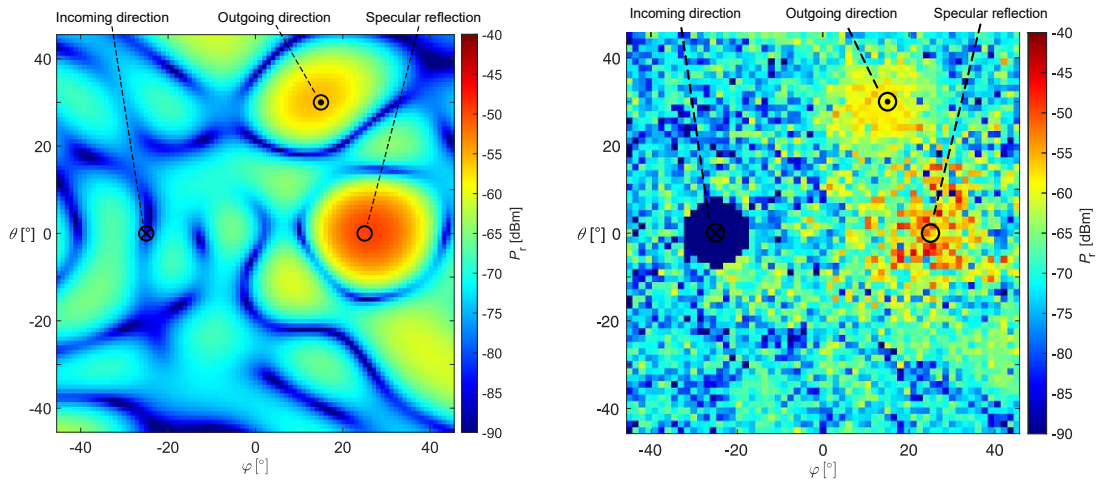

(a) Simulation using AIT Ray Tracer.

(b) Measurements from [11].

Figure 5.2: Received signal power $P_\mathrm{r}(\phi, \theta)$ in azimuth ϕ and elevation θ for an active RIS with 37 elements in reflective mode, configured to focus the reflected signal toward the outgoing direction $(\phi, \theta) = (15°, 30°)$ from an incoming direction $(-25°, 0°)$. The results obtained with numerical simulation using the AIT Ray Tracer are shown in (a) and were compared to empirical measurement data in (b). Due to the physical size of the antennas, points close to the direction of the incoming signals were not measured in (b).

the specular reflection of approximately $-40\,\mathrm{dBm}$ is distinctly present in simulation and measurement as the elements only can provide amplification, as opposed to the 180° phase shift that is required to destructively interfere with the specular reflection. Finally, the outgoing signal toward the desired direction $(15°, 30°)$ has a signal power of approximately $-43\,\mathrm{dBm}$ in both simulation and measurement. The Ray Tracer thus produces good results also for active RISs.

5.2.3 Numerical Evaluation

To further verify the implementation of the path loss model, we implemented a simple beam pattern simulation in MATLAB based on Equation (3.11), i.e., the path loss model described in [10]. The correlation coefficient and errors between the two beam pattern implementations are summarized in Table 5.1, and the absolute difference $P_\mathrm{diff} = |P^\mathrm{ref} - P^\mathrm{RT}|$ for each sample point is plotted in Figure 5.4 for the RIS operating in reflective and active mode. Furthermore, the MAPE is plotted for each sample point in Figure 5.5 for both modes.

To derive the RIS path loss model in [10], it was assumed that the polarization of the Tx and Rx were properly matched even after reflection by the RIS. Furthermore, it was assumed that the antennas could be modeled with the directional antenna model

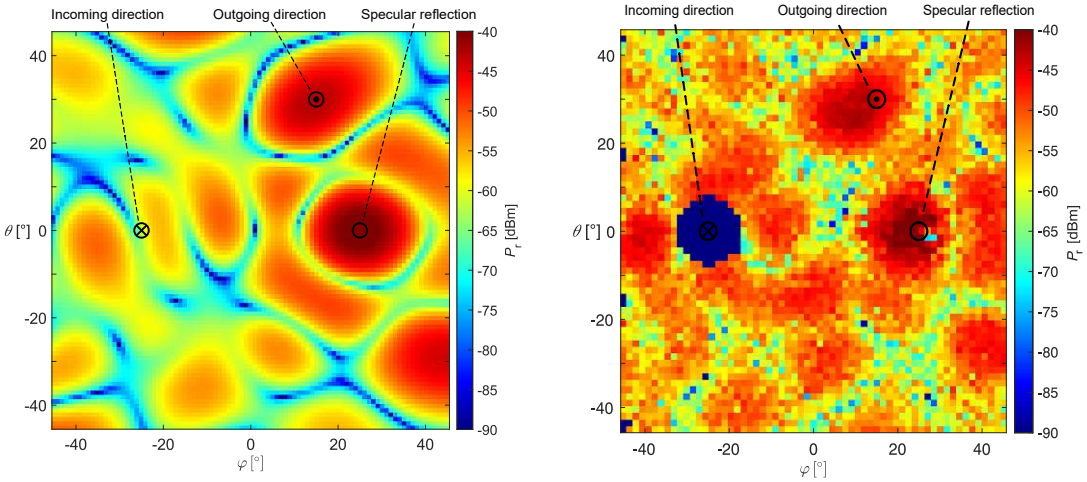

(a) Simulation using AIT Ray Tracer.

(b) Measurements from [11].

Figure 5.3: Received signal power $P_\mathrm{r}(\phi, \theta)$ in azimuth ϕ and elevation θ for an active RIS with 37 elements in active mode, configured to focus the reflected signal toward outgoing direction $(\phi, \theta) = (15°, 30°)$ from an incoming direction $(-25°, 0°)$. The results obtained with numerical simulation using the AIT Ray Tracer are shown in (a) and were compared to empirical measurement data in (b). Due to the physical size of the antennas, points close to the direction of the incoming signals were not measured in (b).

described in Section 3.1.4, that there was LOS between Tx-RIS-Rx, and that there were no additional MPCs than the reflections from the RIS elements. Under these assumptions, our model reduces to the reference model (3.11) and is therefore expected to yield the same results. As the scenario in question fulfilled the assumptions, the results of the two implementations were almost identical, with MAPE of 0.042% for both cases. The MSEs were $2.643 \cdot 10^{-20}$ in reflective mode and $3.508 \cdot 10^{-18}$ in active mode.

Figure 5.4 shows the absolute difference in received signal power between the two implementations. In both reflective and active modes, the largest differences are seen at $(\phi, \theta) = (25°, 0°)$, i.e., in the direction of specular reflection. Additionally, there exist slightly larger differences in the outgoing direction $(15°, 30°)$ in both modes and at $(42°, -29°)$ in the active mode. This corresponds to the most prominent lobes in the beam patterns, in other words, the largest errors appeared where the received signal power was the highest. In alignment with this observation, Figure 5.5 shows that the MAPE is consistently low, at $\leq 0.5\%$ for nearly every point in the obtained results.

5.3 Reflective Environment

In the simulation of the RIS operating in active mode, we saw that the beam pattern had several side lobes with significant signal strength. Many components had a much higher

Table 5.1: Quantitative comparison of numerical beam pattern simulation tools for an RIS operating in reflective and active mode. The beam pattern obtained by simulating the RIS in an anechoic chamber using the AIT Ray Tracer was compared to a MATLAB simulation software based on the path loss model from [10].

	Reflective Mode	**Active mode**
Mean square error	$2.643 \cdot 10^{-20}$	$3.508 \cdot 10^{-18}$
Mean absolute percentage error	0.042%	0.042%

signal strength than that of the intended outgoing direction in reflective mode. In the isolated environment, strong components in other directions than that of the Rx should have no effect on the electric field at the Rx. In a realistic environment, however, strong signal components from the RIS may reflect and interact with the surroundings before reaching the Rx, in particular for active RISs as they may have several strong side lobes. It is thus of great interest to consider the impact of reflective paths between the RIS and the Rx. The implementation of RIS reflections was presented in Section 3.2.3, and the simulation setup for RIS in a reflective environment was described in Section 4.2. In this section, we present the obtained results of the Ray Tracer through a comparison of path visualization and received signal power between two simulations: one in which reflections from the RIS are taken into account, and one in which only RIS rays with a direct path between RIS and Rx are considered.

5.3.1 Ray Launching

For verification of the RIS reflection support implementation, we inspected the generated paths using the path visualization MATLAB program. We inspected two scenarios with and without reflections from RIS, with antennas positioned at $\underline{\boldsymbol{T}} = (1.10, 2.19, 0.5)$ and $\underline{\boldsymbol{R}} = (1.25, 1.16, 0.145)$ and an RIS face centered at $\underline{\boldsymbol{U}} = (2.58, 1.4, 0.5)$ with surface normal $\underline{\boldsymbol{n}} = (-1, 0, 0)$. Figures 5.6a and 5.6b show the generated paths from the simulation without reflections from RIS and with reflections from RIS up to the second order, respectively. We can see a LOS ray directly between Tx and Rx in both simulations, as we omitted the blocking panel from the geometry to reduce the number of intersection checks and improve performance. Additionally, both simulations had two specularly reflected rays that reached the Rx after intersection with the surfaces to the left and right of the RIS.

As with RIS in an anechoic chamber, the simulation which did not consider reflections launched exactly one ray toward each of the 127 RIS elements, marked in red. Upon intersection with the RIS, the rays were relaunched toward the Rx. We additionally confirmed in post-processing that for every sample point in the defined range, exactly 127 rays of RIS type were generated by the Tx and received by the Rx.

In addition to the expected direct rays generated in the non-reflective simulation,

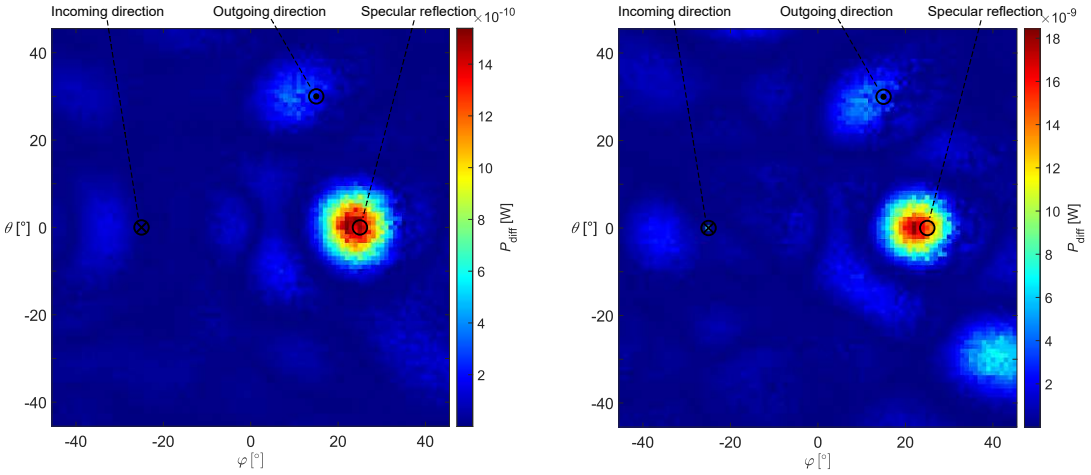

(a) Reflective mode

(b) Active mode

Figure 5.4: The absolute difference in received signal power between the Ray Tracer simulation of RIS in an anechoic chamber and the MATLAB beam pattern simulation software based on (3.11). The RIS is centered at the origin with incoming direction $(\phi, \theta) = (25°, 0°)$ and outgoing direction $(15°, 30°)$.

the reflective simulation identified additional reflection points toward which rays were relaunched after intersection with the RIS. For the configuration and given geometry in Figure 5.6, three first-order reflections and one second-order reflection were identified between the RIS center point and the Rx. Thus, an additional 508 rays of RIS type were launched from the Tx toward their corresponding element. After intersection with the RIS, each ray was relaunched to the target point computed using the image method for the identified permutations, and thereafter specularly reflected on the walls until the Rx was reached. Evidently, the extended ray launching for RIS reflections and the identification of reflection points were implemented as intended and showed the expected behavior in simulation.

It is worth emphasizing that the identified reflections from RIS to Rx, as with any phenomena, depended on the environment and location of Tx and Rx. Therefore, the number of identified paths differed between points in the defined range. Furthermore, certain configurations yielded valid reflection points close to surface edges, in which case the rays from a subset of elements were blocked by another surface or missed the geometry altogether.

5.3.2 Received Signal Power

We analyzed the influence of reflections from the RIS by computing and plotting the received signal power in the defined XY-plane for every sampling point. The received signal power was computed by applying Equations (5.1) to (5.3) to every MPC of RIS

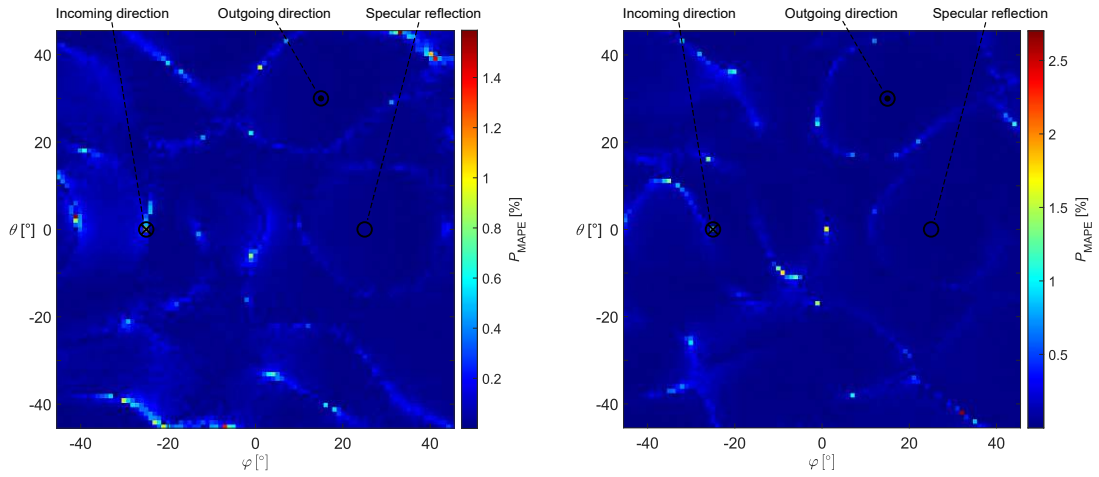

(a) Reflective mode

(b) Active mode

Figure 5.5: The MAPE of received signal power from simulation of RIS in an anechoic chamber using the AIT Ray Tracer, against the MATLAB beam pattern simulation software based on (3.11). The RIS is centered at the origin with incoming direction $(\phi, \theta) = (25°, 0°)$ and outgoing direction $(15°, 30°)$.

type.

In Figures 5.7a and 5.7b the signal power is plotted for the non-reflective and reflective simulation, respectively. The RIS placed at $\underline{\boldsymbol{U}} = (2.58, 1.4, 0.5)$ reflected the signal from above the top right corner of the plot, with an outgoing direction toward the Rx at $\underline{\boldsymbol{R}} = (1.25, 1.16, 0.145)$. Thus, the non-reflective plot in Figure 5.7a depicts a diagonal cut through the beam pattern of the RIS for the given configuration. The strongest component in the XY-plane was a $1 \times 0.3\,\mathrm{m}$ large region centered around the outgoing direction, with a received signal power from -55 to $-45\,\mathrm{dBm}$. Additionally, there were two smaller and weaker side lobes of $-51\,\mathrm{dBm}$ centered at $(x, y) = (1.9, 1)\,\mathrm{m}$, and $-56\,\mathrm{dBm}$ centered at $(1.25, 1.4)\,\mathrm{m}$.

The simulation considering reflections from the RIS up to the second order generated the plot seen in Figure 5.7b. Although the results evidently correlate, the constructive and destructive interference from reflected components can be clearly distinguished at several points in the plot. The outgoing direction makes up the strongest component with a received signal power from approximately -58 to $-44\,\mathrm{dBm}$, thus showing a slight difference in received signal strength compared to the simulation that only considers direct paths between the RIS and Rx. In the intended outgoing direction, the reflections caused a small relative change in signal strength of $0.3\,\mathrm{dB}$. At other locations, such as the poor coverage areas in the bottom right part of the XY-plane, the reflected components significantly improved the received power.

The difference between the two results

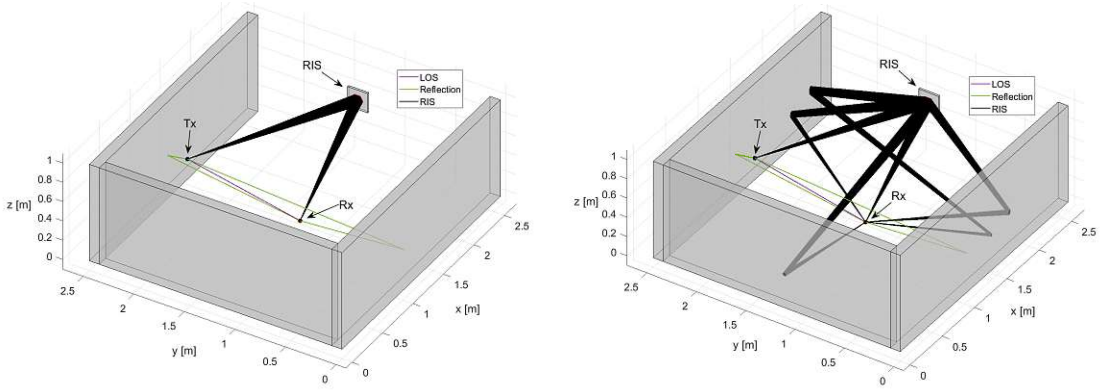

(a) Maximum RIS reflection order $n_{\max}^{\text{RIS}} = 0$. (b) Maximum RIS reflection order $n_{\max}^{\text{RIS}} = 2$.

Figure 5.6: Path visualization for an RIS with 127 elements in a reflection environment with $\underline{\boldsymbol{T}} = (1.10, 2.19, 0.5)$ and $\underline{\boldsymbol{R}} = (1.25, 1.16, 0.145)$. The LOS ray is depicted in purple, specularly reflected rays in green, RIS rays in black, and globally mapped RIS element points in red.

$$\Delta P_{\text{r}}^{\text{dB}} = 10 \log_{10} \left(\frac{P_{\text{reflections}}}{P_{\text{isolated}}} \right) \tag{5.6}$$

was computed and plotted in Figure 5.7c. The maximum constructive interference from reflections caused a 45.87 dB difference in received signal power at $(1.3, 0.68)$ m where the direct signal from the RIS was below the noise floor of -105 dBm, but with reflections reached -60 dBm. The maximum destructive interference from reflections caused a -35.9 dB difference at $(1.58, 0.48)$ m with a direct signal from the RIS of -66.6 dBm, and -102.5 dBm with destructive interference from reflections.

Finally, the squared error $(P_{\text{reflections}} - P_{\text{isolated}})^2$ at each point was plotted in Figure 5.7d, showing that the largest absolute difference in received signal strength was observed primarily in the strong component centered around the intended outgoing direction, and by the reflected components in the bottom right part of the plane.

The wave pattern in Figure 5.7b should not be confused with the wave pattern of the carrier frequency with wavelength $\lambda = 1.16$ cm. Due to the chosen sampling size of 2 cm, the plot suffers from aliasing. To demonstrate this, we performed a high-resolution simulation of a smaller section of the XY-plane with a sampling distance of 0.2 cm. The results are plotted in Figure 5.8, clearly showing the small-scale fading with constructive and destructive interference at approximately every $\frac{\lambda}{2}$.

We see that the reflections from the RIS can have a large impact on the received signal power, showing the importance of considering them for an accurate simulation of RISs. The benefit of our compartmentalized model is thus evident, as it allows for simple incorporation of additional features to accurately model the impact of RISs on realistic and complex environments.

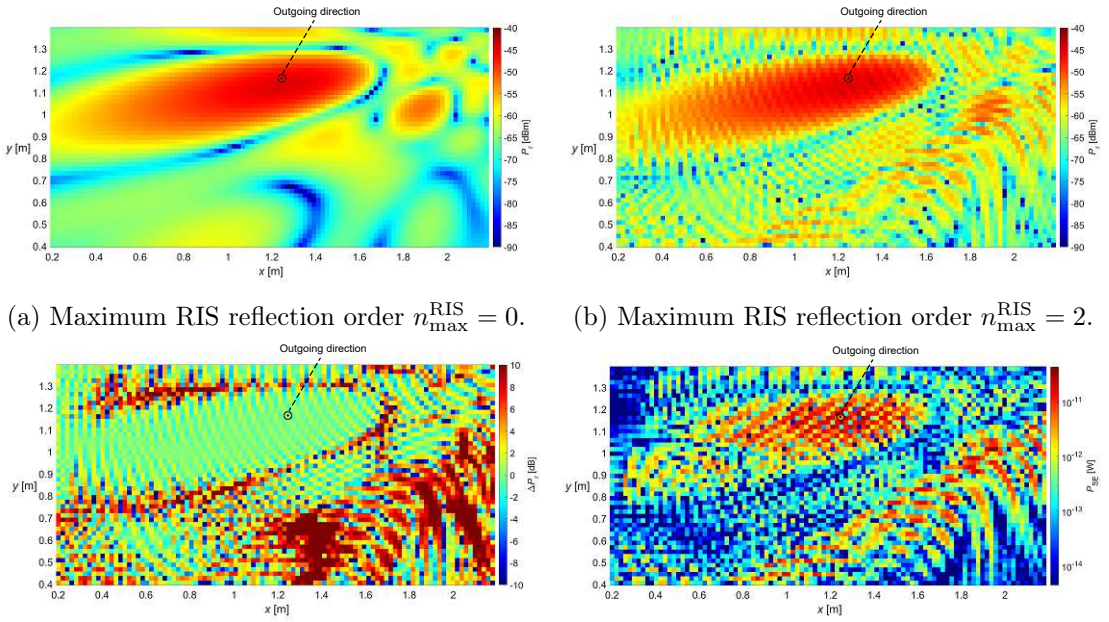

(a) Maximum RIS reflection order $n_{\max}^{\text{RIS}} = 0$.

(b) Maximum RIS reflection order $n_{\max}^{\text{RIS}} = 2$.

(c) $\Delta P_{\text{r}}^{\text{dB}}$

(d) Squared error

Figure 5.7: Received signal power P_{r} for simulation of an active RIS in the AIT Ray Tracer, considering in (a) only direct signal components from the RIS, and (b) direct and reflected signal components from the RIS. The difference in received power between the two simulations is plotted in (c), and the squared error in (d).

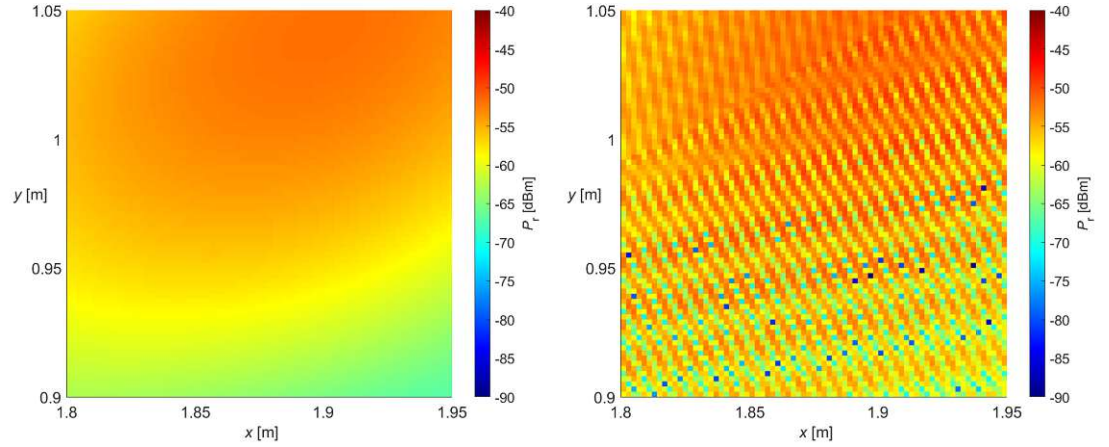

(a) Maximum RIS reflection order $n_{\max}^{\text{RIS}} = 0$.

(b) Maximum RIS reflection order $n_{\max}^{\text{RIS}} = 2$.

Figure 5.8: Received signal power P_{r} for a high-resolution simulation of an active RIS in the AIT Ray Tracer, considering direct and reflected signal components from the RIS.

Chapter 6

Conclusion

With the extreme growth in global mobile data traffic, the development of 6G mobile communication networks is essential to support the demand for reliable and secure wireless connections with higher data rates and lower latencies. The higher frequency bands that are suggested to tackle the spectrum shortage come with several challenges due to the high propagation loss and strong attenuation of blocked transmission paths.

Wireless communication channels are traditionally viewed as an uncontrollable system that negatively impacts the quality of the signal as it interacts with the environment. Reconfigurable intelligent surfaces (RISs), however, enable the environment to actively assist information transfer. By manipulating the signal in real-time in order to constructively or destructively interfere at desired locations, RISs offer promising solutions to the propagation issues for mmWaves, making it an important enabling technology for 6G wireless networks.

For the development of RISs, accurate models and numerical simulation tools are of great importance. An efficient and accurate technique for wireless channel modeling is ray tracing, which approximates electromagnetic waves as rays following the laws of geometrical optics and can be easily accelerated using GPUs. The goal of this thesis is to extend the GPU-accelerated Ray Tracer from the AIT Austrian Institute of Technology to support the effects of reconfigurable intelligent surfaces in complex environments.

To provide the necessary theory and concepts in the relevant areas, an introduction to wireless communication channels, electromagnetic wave propagation mechanisms, and reconfigurable intelligent surfaces was given. We further discussed ray tracing for wireless communication from both a conceptual and an algorithmic perspective, and introduced the workflow of the NVIDIA OptiX ray tracing engine upon which the AIT Ray Tracer is built.

The AIT Ray Tracer is developed to efficiently and accurately simulate the propagation of electromagnetic waves, using a two-stage hybrid ray tracing method to overcome the limitations of the shooting and bouncing ray method and the image method. In the first stage, potential reflection, diffraction, and diffuse scatter points from the transmitter to the receiver are computed using cheap analytical algorithms on the CPU. In the second stage, rays are launched toward the precomputed points and traced on the GPU, ensuring that only rays that reach the receiver are accounted for in the results. The Ray Tracer supports a range of antenna implementations and is capable of simulating stationary and non-stationary scenarios in complex environments. Furthermore, additional features and models are easily incorporated into the Ray Tracer due to its modular architecture.

We propose an approach for the integration of reconfigurable intelligent surfaces in

the Ray Tracer by launching rays toward the individual RIS antenna elements which are manipulated and reflected upon intersection with the RIS. For the evaluation of the electric field, we start from an RIS path loss model proposed by Tang, 2022. The model was compartmentalized for improved flexibility and better compatibility with the AIT Ray Tracer. Additionally, our model allows for a fully reflective environment and can therefore be integrated into complex scenarios. We demonstrated this by extending the Ray Tracer to support higher-order reflected paths through the RIS.

To verify and evaluate our implementation, we performed two simulations. The first scenario evaluated the beam pattern of an RIS in an anechoic environment and was verified by comparison to measurements and a rudimentary numerical simulation software based on the model proposed by Tang in 2022. The correctness of our implementation was verified, and the model yielded reliable results for all the simulated and measured cases. The second scenario considered the RIS in a reflective environment and was evaluated using our path visualization tool. We showed that the compartmentalization of our model successfully enabled the extension to advanced propagation mechanisms. Furthermore, we found that higher-order reflected components from the RIS on the environment have a significant effect on the received signal strength, indicating that the extensions enabled by our model play an important role in the accurate modeling of reconfigurable intelligent surfaces.

While providing a full description of RISs, our implementation decouples the effects of the RIS from other components in the environment, revealing the impact on the electric field upon each interaction with the scene. Thus, we are not limited to multi-path components with line-of-sight between the antennas and the RIS, and we do not rely on specific environmental requirements or antenna representations. Consequently, our approach enables future work to improve the accuracy of RISs in wireless channel models, for instance, by incorporating polarization or diffractions from the RIS.

Bibliography

[1] F. Tariq, M. R. A. Khandaker, K.-K. Wong, M. A. Imran, M. Bennis, and M. Debbah, "A Speculative Study on 6G," *IEEE Wireless Communications*, vol. 27, no. 4, pp. 118–125, 2020.

[2] T. S. Rappaport, Y. Xing, O. Kanhere, S. Ju, A. Madanayake, S. Mandal, A. Alkhateeb, and G. C. Trichopoulos, "Wireless Communications and Applications Above 100 GHz: Opportunities and Challenges for 6G and Beyond," *IEEE Access*, vol. 7, pp. 78729–78757, 2019.

[3] I. F. Akyildiz, C. Han, and S. Nie, "Combating the Distance Problem in the Millimeter Wave and Terahertz Frequency Bands," *IEEE Communications Magazine*, vol. 56, no. 6, pp. 102–108, 2018.

[4] E. Björnson, Ö. Özdogan, and E. G. Larsson, "Reconfigurable Intelligent Surfaces: Three Myths and Two Critical Questions," *IEEE Communications Magazine*, vol. 58, no. 12, pp. 90–96, 2020.

[5] E. Basar, M. Di Renzo, J. De Rosny, M. Debbah, M.-S. Alouini, and R. Zhang, "Wireless Communications Through Reconfigurable Intelligent Surfaces," *IEEE Access*, vol. 7, pp. 116753–116773, 2019.

[6] J. Hu, H. Zhang, B. Di, L. Li, K. Bian, L. Song, Y. Li, Z. Han, and H. V. Poor, "Reconfigurable Intelligent Surface Based RF Sensing: Design, Optimization, and Implementation," *IEEE Journal on Selected Areas in Communications*, vol. 38, no. 11, pp. 2700–2716, 2020.

[7] A. F. Molisch, *Wireless Communications: From Fundamentals to Beyond 5G*. IEEE Press, Wiley, 2022.

[8] Z. Yun and M. F. Iskander, "Ray Tracing for Radio Propagation Modeling: Principles and Applications," *IEEE Access*, vol. 3, pp. 1089–1100, 2015.

[9] B. Rainer, D. Löschenbrand, S. Zelenbaba, M. Hofer, and T. Zemen, "Towards a Non-Stationary Correlated Fading Process for Diffuse Scattering in Ray Tracing," in *IEEE 31st Annual International Symposium on Personal, Indoor and Mobile Radio Communications*, 2020.

[10] W. Tang, X. Chen, M. Z. Chen, J. Y. Dai, Y. Han, M. D. Renzo, S. Jin, Q. Cheng, and T. J. Cui, "Path Loss Modeling and Measurements for Reconfigurable Intelligent Surfaces in the Millimeter-Wave Frequency Band," *IEEE Transactions on Communications*, vol. 70, no. 9, pp. 6259–6276, 2022.

[11] H. Radpour, M. Hofer, L. W. Mayer, A. Hofmann, M. Schiefer, and T. Zemen, "Active Reconfigurable Intelligent Surface for the Millimeter-Wave Frequency Band: Design and Measurement Results," 2023, arXiv, submitted.

[12] F. Mani and K. Haneda, *Improved Ray-Tracing for Advanced Radio Propagation Channel Modeling*. PhD thesis, Université Catholique de Louvain, 2012.

[13] M. Gan, *Accurate and Low-complexity Ray Tracing Channel Modeling*. PhD thesis, Technical University of Vienna, 2015.

[14] B. Saleh and M. Teich, *Fundamentals of Photonics*. Wiley Series in Pure and Applied Optics, Wiley, 2007.

[15] K. Zhi, C. Pan, H. Ren, K. K. Chai, and M. Elkashlan, "Active RIS Versus Passive RIS: Which is Superior With the Same Power Budget?," *IEEE Communications Letters*, vol. 26, no. 5, pp. 1150–1154, 2022.

[16] V. Degli-Esposti, E. M. Vitucci, M. D. Renzo, and S. A. Tretyakov, "Reradiation and Scattering From a Reconfigurable Intelligent Surface: A General Macroscopic Model," *IEEE Transactions on Antennas and Propagation*, vol. 70, no. 10, pp. 8691–8706, 2022.

[17] A. S. Glassner, *An Introduction to Ray Tracing*. The Morgan Kaufmann Series in Computer Graphics, Elsevier Science, 1988.

[18] M. Born, E. Wolf, and A. Bhatia, *Principles of Optics: Electromagnetic Theory of Propagation, Interference and Diffraction of Light*. Cambridge University Press, 2000.

[19] H. Ling, R.-C. Chou, and S.-W. Lee, "Shooting and Bouncing Rays: Calculating the RCS of an Arbitrarily Shaped Cavity," *IEEE Transactions on Antennas and Propagation*, vol. 37, no. 2, pp. 194–205, 1989.

[20] V. Degli-Esposti, F. Fuschini, E. M. Vitucci, and G. Falciasecca, "Speed-Up Techniques for Ray Tracing Field Prediction Models," *IEEE Transactions on Antennas and Propagation*, vol. 57, no. 5, pp. 1469–1480, 2009.

[21] S. Tan and H. Tan, "A Microcellular Communications Propagation Model Based on the Uniform Theory of Diffraction and Multiple Image Theory," *IEEE Transactions on Antennas and Propagation*, vol. 44, no. 10, pp. 1317–1326, 1996.

[22] M. A. Meselhi, S. M. Elsayed, D. L. Essam, and R. A. Sarker, "Fast Differential Evolution for Big Optimization," in *11th International Conference on Software, Knowledge, Information Management and Applications (SKIMA)*, 2017.

[23] S. G. Parker, J. Bigler, A. Dietrich, H. Friedrich, J. Hoberock, D. Luebke, D. McAllister, M. McGuire, K. Morley, A. Robison, and M. Stich, "OptiX: A General Purpose Ray Tracing Engine," *ACM Transactions on Graphics*, August 2010.

[24] R. Kouyoumjian and P. Pathak, "A Uniform Geometrical Theory of Diffraction for an Edge in a Perfectly Conducting Surface," *Proceedings of the IEEE*, vol. 62, no. 11, pp. 1448–1461, 1974.

[25] V. Degli-Esposti, F. Fuschini, E. M. Vitucci, and G. Falciasecca, "Measurement and Modelling of Scattering From Buildings," *IEEE Transactions on Antennas and Propagation*, vol. 55, no. 1, pp. 143–153, 2007.

[26] W. Stutzman and G. Thiele, *Antenna Theory and Design*. Antenna Theory and Design, Wiley, 2012.

[27] C. Balanis, *Antenna Theory: Analysis and Design*. John Wiley & Sons, 2005.

[28] W. Tang, M. Z. Chen, X. Chen, J. Y. Dai, Y. Han, M. Di Renzo, Y. Zeng, S. Jin, Q. Cheng, and T. J. Cui, "Wireless Communications With Reconfigurable Intelligent Surface: Path Loss Modeling and Experimental Measurement," *IEEE Transactions on Wireless Communications*, vol. 20, no. 1, pp. 421–439, 2021.

Acronyms

5G fifth-generation cellular network. 1

6G sixth-generation cellular network. iii, 1, 59

AIT AIT Austrian Institute of Technology. i, iii, vii, 2, 6, 12, 21, 22, 27, 28, 30, 31, 37, 40, 44, 47, 49–53, 55, 57, 59, 60

CIR channel impulse response. 34, 42, 48

CPU central processing unit. vii, 16–18, 22, 23, 26, 47, 59, 67

CTF channel transfer function. 48

DSD Doppler spectral density. 48

EM electromagnetic. iii, 1, 2, 5, 13, 21, 37, 38, 59

FDTD finite-difference time-domain. 2

FEM finite element method. 2

GPU graphics processing unit. iii, vii, 2, 16–18, 21–23, 26, 59, 67

IO interacting object. 5, 34, 38

IoT internet of things. 1

LOS line-of-sight. 5, 7, 25, 26, 30, 31, 37, 38, 47–50, 52, 53, 56, 60

M2M machine-to-machine. 1

MAPE mean absolute percentage error. vii, 49, 51–53, 55

mmWave millimeter-wave frequency. 1, 42, 59

MPC multi-path component. 5, 21, 26, 27, 30, 33, 37, 42, 47–49, 52, 54, 60

MSE mean square error. 48, 49, 52, 53

NLOS non-line-of-sight. 1

OSM OpenStreetMap. 23, 25

PDP power delay profile. 48

PEC perfect electrical conductor. 43

RIS reconfigurable intelligent surface. iii, vii–ix, 1, 2, 5, 11, 12, 21, 28–35, 37–57, 59, 60

RT Ray Tracer. iii, vii, 2, 6, 12, 21–23, 26–31, 33, 37–41, 43, 44, 47–55, 57, 59, 60

Rx receiver. 5–7, 9–12, 14, 15, 21, 23, 25–30, 32–35, 37–45, 47–49, 51–55, 59

SBR shooting and bouncing ray. vii, 14, 15, 28, 59

SNR signal-to-noise ratio. 1

Tx transmitter. 5–7, 9, 10, 12, 14, 21, 23, 25–30, 32, 34, 37–46, 48, 49, 51–54, 59

UTD uniform theory of diffraction. 9, 10, 23, 26

ZAG z-aligned axis geometry. vii, 23–25, 29, 38, 40, 43, 44

Glossary

anechoic chamber an isolated room designed to prohibit reflections of electromagnetic waves. vii, 34, 37, 38

buffer a multidimensional array that can be bound to a variable, used to store data during ray tracing. 18, 19

context an instance of a running OptiX engine. 22

device the GPU and its associated memory in a CUDA C++ program. 18, 47

host the CPU and its associated memory in a CUDA C++ program. 17–19, 47

kernel a function that is executed in parallel on the device. 18

primitive the smallest geometric unit of processing in the scene. 18

relay a device used to receive, amplify, and retransmit signals between different parts of a network. 1